



A Physically Admissible Stokes Vector Reconstruction in Linear Polarimetric Imaging

Carole Le Guyader¹ · Samia Ainouz² · Stéphane Canu²

Received: 7 December 2021 / Accepted: 24 December 2022 / Published online: 11 January 2023
© The Author(s), under exclusive licence to Springer Science+Business Media, LLC, part of Springer Nature 2023

Abstract

Polarization encoded images improve on conventional intensity imaging techniques by providing access to additional parameters describing the vector nature of light. In a polarimetric image, each pixel is related to a 4×1 vector named Stokes vector (3×1 in a linear configuration, which is the framework retained afterwards). Such images comprise a valuable set of physical information on the objects they contain, amplifying subsequently the accuracy of the analysis that can be done. A Stokes imaging polarimeter yields data named radiance images from which Stokes vectors are reconstructed, supposed to comply with a physical admissibility constraint. Classical estimation techniques such as pseudo-inverse approach exhibit defects, hampering any relevant physical interpretation of the scene: (i) first, due to their sensitivity to noise and errors that may contaminate the observed radiance images and that may then propagate to the evaluation of the Stokes vector components, thus justifying an ad hoc a posteriori treatment of Stokes vectors; (ii) second, in not taking this physical admissibility criterion explicitly into account. Motivated by this observation, the proposed contribution aims to provide a method of reconstruction addressing both issues, thus ensuring smoothness and spatial consistency of the reconstructed components, as well as compliance with the prescribed physical admissibility constraint. A by-product of the algorithm is that the resulting angle of polarization reflects more faithfully the physical properties of the materials present in the image. The mathematical formulation yields a non-smooth convex optimization problem that is then converted into a min–max problem and solved by the generic Chambolle–Pock primal–dual algorithm. Several mathematical results (such as existence/uniqueness of the minimizer of the primal problem, existence of a saddle point to the associated Lagrangian, etc.) are supplied and highlight the well-posed character of the modelling. Experiments demonstrate that our method provides significant improvements (i) over the least square-based method both in terms of quantitative criteria (physical admissibility constraint automatically met) and qualitative assessment (spatial regularization/coherency), (ii) over the physical consistency of related relevant polarimetric parameters such as the angle and degree of polarization, (iii) robustness of the method when applied on real outdoor scenes acquired in degraded conditions (poor weather conditions, etc.).

Keywords Polarimetric imaging · Stokes vectors · Proximal algorithms · Min–max problem

Mathematics Subject Classification 68U10 · 49 · 65K

✉ Carole Le Guyader
carole.le-guyader@insa-rouen.fr
Samia Ainouz
samia.ainouz@insa-rouen.fr
Stéphane Canu
stephane.canu@insa-rouen.fr

¹ LMI, INSA Rouen Normandie, Normandie Université, 685 Avenue de l'Université, 76800 Saint-Étienne-du-Rouvray, France

1 Introduction

In the following, we place ourselves in the context of linear Stokes polarimetry. Note, however, that the modelling can be straightforwardly extended to the full Stokes framework. The only scientific obstacle we have identified is the computation load: indeed, some stages of the algorithm may not be

² LITIS, INSA Rouen Normandie, UNIROUEN, UNIHAVRE, Normandie Université, 685 Avenue de l'Université, 76800 Saint-Étienne-du-Rouvray, France

stated in closed-form solutions; in particular, if the involved subproblems are not separable with respect to the unknowns, requiring thus additional iterative loops.

Besides, we would like to emphasize that the proposed method abstracts from the type of acquisition equipment used and is therefore intended to be applied independently of the hardware aspect. The contribution is thus more methodologically oriented and not dedicated to an exhaustive comparison of the performance of different materials. Our experimental protocol was naturally dictated by the material resources at our disposal at the time of writing the manuscript. It turns out to be basic indeed (better performing cameras with specialized chip have been put on the market); we believe that having worked within a fairly simple framework allows for a more unbiased evaluation of the method, related more to the quality of the mathematical model than to the material framework used.

Polarization images, obtained from Stokes vector computation, are a non-conventional modality in which each reflected wave from a pixel is strongly linked to the physical properties of the surface it impinges on. It is thus a rich modality that enables one to characterize an object by its reflective properties: indeed, in such an image, each pixel encodes information regarding the object intensity, its roughness, its orientation and its reflection [1]. This modality is increasingly used in applications ranging from indoor autonomous navigation [2], depth map estimation [3], 3D object reconstruction [4,5], to differentiation of healthy and unhealthy cervical tissues in order to detect cancer at an early stage [6]. Recently, polarization imaging was exploited in autonomous driving applications, either to enhance car detection [7], road mapping and perception [8], or even to detect road objects in adverse weather conditions [9]. While literature claims the high informative character of polarization, it tends to hide two important scientific barriers [10]: (i) first, Stokes vectors are estimated from radiance measurements that might be corrupted by noise and errors, even if current acquisition systems are calibrated to reduce their impact. These might then be transferred to the prediction of Stokes vectors; (ii) second, in classical reconstruction methods such as pseudo-inverse approach, Bayesian approaches [11,12] or smoothly varying reconstructions [13], the physical admissibility constraint is not explicitly enforced, making erroneous any physical interpretation of the content.

Thus, in this paper and in the context of automatic linear polarization image acquisition, we address the issue of estimating the Stokes vectors with prescribed polarization physical constraints and prescribed regularity, ensuring homogeneity of the vector constituents while preserving sharp edges. To achieve this goal, the set of Stokes vectors is viewed as the minimal argument (uniqueness holds here) of a specifically designed cost function that encodes a couple of geometrical criteria in addition to the data fitting

term (phrased as a classical L^2 -norm as will be seen below): compliance with the prescribed physical admissibility condition through inequality constraints (*i.e.* hard constraints) and spatial consistency through a joint total variation term increasing the relevancy of the resulting angle of polarization that reflects more faithfully the physics of the scene. Inspired by prior related works by Chambolle and Pock [14] dedicated to primal-dual algorithms, the optimization problem is then restated as a min–max one using the dual formulation of the introduced coupled total variation. Extensive evaluations are conducted on real indoor/outdoor scene possibly degraded images, including accuracy/relevancy with respect to two polarimetric parameters, the degree of polarization (that ensures the physical admissibility of the estimated Stokes vectors) and the angle of polarization (allowing the assessment of the physical consistency of the scene), and the suitability of joint total variation in comparison with an uncoupling term. The estimated Stokes vectors exhibit realistic physical properties and might be used for any polarization imaging application.

To summarize, our contributions are of different kinds: (i) first, of a methodological nature that frees from the type of material employed. Several criteria (compliance with the physical admissibility constraint, spatial coherency enforcement, coupling of the channels, etc.) are intertwined in the design of a cost function whose minimal argument is the sought set of reconstructed Stokes vectors; (ii) second, of a more theoretical nature, by devising a constrained optimization problem for which the existence/uniqueness of a minimizer is ensured, together with a computationally tractable algorithm including closed-form solutions at each step. Several theoretical results are provided (existence of a saddle point, convergence result, etc.), guaranteeing the well-posed character of the introduced model; (iii) at last, of a more applied nature, with extensive evaluations on real scene images including accuracy with respect to classical quantitative metrics, qualitative assessment, comparisons with standard strategies and conformity with physical reality.

2 Polarization Formalism and Motivations for the Introduction of the Proposed Model

Before stating our problem, we review some pieces of polarization and Stokes–Mueller formalism.

Light waves can oscillate in more than one orientation. Polarization represents the direction of propagation of the light wave electrical field. When the direction is linear, elliptical or circular, the polarization state is said to be totally polarized, while it is said to be partially polarized or non-polarized when the light wave partly propagates in a random way [15]. Polarimetric imaging consists in representing the polarization state of the light wave reflected according to each

pixel of the image, which gives a cue of the material properties of the surface, its orientation and its shape. The linear part of the reflected light can be described by measurable parameters embedded in the so-called linear Stokes vector $S = (S_0, S_1, S_2)^T$ where $S_0 > 0$ represents the total intensity, S_1 the amount of horizontally and vertically linearly polarized light, and S_2 the quantity of diagonally linearly polarized light. By construction, the Stokes vector is physically admissible if and only if the two following conditions are fulfilled:

$$S_0 > 0 \quad \text{and} \quad S_0^2 \geq S_1^2 + S_2^2. \tag{1}$$

In the following, for theoretical purposes, we slightly relax the former condition and convert it into a non-strict inequality, *i.e.* $S_0 \geq 0$ (the weakening of this condition not being an obstacle as demonstrated in [16]). Other properties can be derived from the Stokes vectors, the most important ones being the Degree Of Linear Polarization (DOLP) [17] and the Angle Of Linear Polarization AOLP defined, respectively, by:

$$\text{DOLP} = \frac{\sqrt{S_1^2 + S_2^2}}{S_0} \quad \text{and} \quad \text{AOLP} = \frac{1}{2} \text{atan2}(S_2, S_1).$$

The DOLP $\in [0, 1]$ describes quantitatively the partial linear polarization of the light beam [18]. It is up to 1 for totally polarized light, 0 for unpolarized light, and between 0 and 1 for partially polarized light. The AOLP $\in]-\frac{\pi}{2}, +\frac{\pi}{2}[$ provides information about the object plane (surface normal) that reflects the incoming light. In the absence of any form of noise, the AOLP should be constant in homogeneous areas.

Polarization images encode the Stokes vectors which are estimated from the acquired radiance images. The acquisition device is composed of a polarizer filter oriented at an angle α between the object and the sensor (camera) [19]. Physically, the Stokes vector represents the reflected light from the object that passes through the polarizer filter before reaching the camera (cf. Fig. 1). To estimate the three components (in the linear configuration), at least three acquisitions with three different angles are required.

To achieve this goal, recent technologies allow for automatic acquisition: the Polarcam 4D Technology polarimetric camera is a commonly used one. Again, we highlight the fact that the scope of the contribution is devoted to methodological aspects and not to an exhaustive comparison of the performance of different materials. This camera provides simultaneously four images, respectively, obtained with four different linear polarizers oriented at $(\alpha_i)_{i=1,\dots,4} = (0^\circ, 90^\circ, 45^\circ, 135^\circ)$. The polarimetric camera measures an intensity $I_p(\alpha_i)$ of the scene for each angle α_i . The relationship between the Stokes vector S_{in} simplified as $S =$

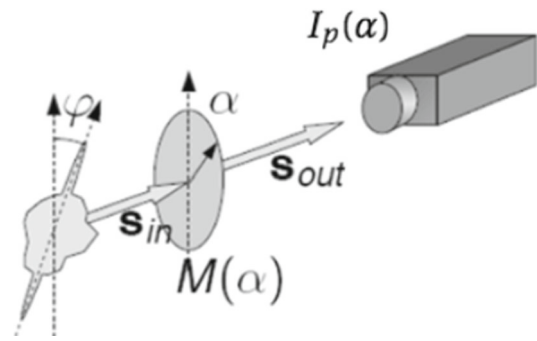


Fig. 1 The polarization device principle

$(S_0, S_1, S_2)^T$, and the intensities $I_p(\alpha_i)_{i=1,\dots,4}$ simplified as I reaching the camera is given by, $\forall i \in \{1, \dots, 4\}$,

$$I_{\alpha_i} = \frac{1}{2} (1 \cos(2\alpha_i) \sin(2\alpha_i)) \begin{pmatrix} S_0 \\ S_1 \\ S_2 \end{pmatrix},$$

which can be rewritten in matrix form as

$$I = AS, \tag{2}$$

where $I = (I_0 \ I_{90} \ I_{45} \ I_{135})^T$ refers to the four intensities according to each angle of the polarizer $(\alpha_i)_{i=1,\dots,4}$ and $A \in \mathbb{R}^{4 \times 3}$ denotes the calibration matrix of the polarization camera defined by:

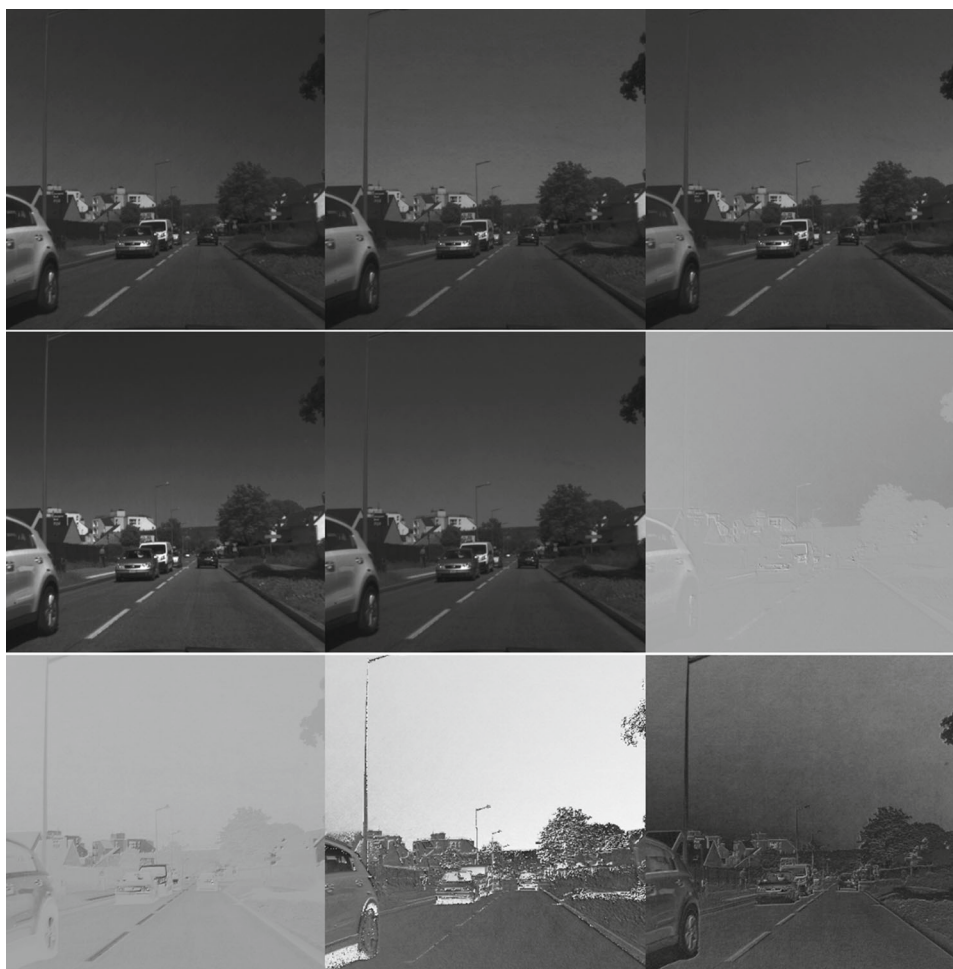
$$A = \frac{1}{2} \begin{pmatrix} 1 & 1 & 0 \\ 1 & -1 & 0 \\ 1 & 0 & 1 \\ 1 & 0 & -1 \end{pmatrix}.$$

Figure 2 shows an example of polarimetric images according to each angle of the polarizer filter.

In order to recover the Stokes vector S , Eq. (2) should be solved, but the system of equations is overdetermined, the number of equations being strictly greater than the number of unknowns. Regardless of the physical admissibility constraints, the most widespread solution in the literature to find an approximate solution to this overdetermined system is the pseudo-inverse approach also called least square method. This leads to introducing the pseudo-inverse of matrix A given by $\tilde{A} = (A^T A)^{-1} A^T \in \mathbb{R}^{3 \times 4}$ to estimate S . The resulting Stokes vector is thus given by the following equation (named normal equation):

$$S = \tilde{A}I = \begin{pmatrix} \frac{1}{2} & \frac{1}{2} & \frac{1}{2} & \frac{1}{2} \\ 1 & -1 & 0 & 0 \\ 0 & 0 & 1 & -1 \end{pmatrix} \begin{pmatrix} I_0 \\ I_{90} \\ I_{45} \\ I_{135} \end{pmatrix}. \tag{3}$$

Fig. 2 Example of polarimetric images. From left to right and top to bottom: I_0 , I_{45} , I_{90} , I_{135} , S_0 , S_1 , S_2 , AOLP, DOLP



Note that with this formula, an approximate solution is found when no exact solution exists, and it gives an exact solution when one does exist, *i.e.* when $I \in \text{Im } A$. The least square approximation is straightforward to apply but has two main drawbacks in the case of polarization formalism. The first issue is that the obtained solution does not take into account the physical admissibility constraint exhibited by the Stokes vectors as defined in Eq. (1). The resulting Stokes components violate these conditions most of the time, entailing erroneous values of the polarization properties (AOLP and DOLP) of the associated pixel. The second issue lies in the pseudo-inverse form. Indeed, to compute back the intensities I from the Stokes parameters of Eq. (3) using Eq. (2), the following equation should hold:

$$I = A\tilde{A}I,$$

which applies if and only if

$$I_0 + I_{90} = I_{45} + I_{135} . \tag{4}$$

Unfortunately, this condition is hard to be fulfilled for each pixel, even with a good camera configuration as it is the case for the Polar4D camera.

To overcome these fundamental shortcomings in polarimetric image acquisition and to be more consistent with the physics, we phrase the Stokes vector reconstruction issue as a constrained optimization problem, implying that the physical admissibility conditions are explicitly enforced. This is the core of the next section, complemented by several theoretical results demonstrating the well-posed character of the model.

3 Mathematical Modelling of the Proposed Reconstruction Model and Theoretical Results

3.1 Definition of the Primal Problem

We start by introducing the discrete setting that we will use throughout the next sections and follow the notations of [20]. To simplify, we view our images as two-dimensional matrices

defined on a regular Cartesian grid \mathcal{G} of size $N \times N$:

$$\mathcal{G} = \{(ih, jh) \mid 1 \leq i \leq N, 1 \leq j \leq N\},$$

h denoting the size of the spacing classically taken to 1, while the indices (i, j) denote the discrete location (ih, jh) in the image domain. The index i is the index associated with the rows (y -direction) whilst j is the index related to the columns (x -direction). Adaptation to other cases is straightforward. We denote by X the Euclidean space $\mathbb{R}^{N \times N}$ equipped with the standard scalar product

$$\langle u, v \rangle_X = \sum_{(i,j) \in \mathcal{G}} u_{i,j} v_{i,j}$$

and the related norm is defined by $\|u\|_X = \sqrt{\langle u, u \rangle_X} = \sqrt{\sum_{(i,j) \in \mathcal{G}} u_{i,j}^2}$.

If $u \in X$, the gradient ∇u is a vector in $Y = X \times X$ defined by $(\nabla u)_{i,j} = \left((\nabla u)_{i,j}^1, (\nabla u)_{i,j}^2 \right)$ with

$$\begin{aligned} (\nabla u)_{i,j}^1 &= \begin{cases} u_{i+1,j} - u_{i,j} & \text{if } i < N \\ 0 & \text{if } i = N \end{cases}, \\ (\nabla u)_{i,j}^2 &= \begin{cases} u_{i,j+1} - u_{i,j} & \text{if } j < N \\ 0 & \text{if } j = N \end{cases}. \end{aligned}$$

We also define a scalar product on Y by

$$\langle p, q \rangle_Y = \sum_{(i,j) \in \mathcal{G}} \left(p_{i,j}^1 q_{i,j}^1 + p_{i,j}^2 q_{i,j}^2 \right),$$

with $p = (p^1, p^2) \in Y$ and $q = (q^1, q^2) \in Y$. The discrete divergence operator $\text{div} : Y \rightarrow X$ (defined analogously to the continuous setting) is the opposite of the adjoint operator of the gradient operator ∇ , that is,

$$\forall p \in Y, \forall u \in X, \langle -\text{div } p, u \rangle_X = \langle p, \nabla u \rangle_Y,$$

div being thus given by

$$\begin{aligned} (\text{div } p)_{i,j} &= \begin{cases} p_{i,j}^1 - p_{i-1,j}^1 & \text{if } 1 < i < N \\ p_{i,j}^1 & \text{if } i = 1 \\ -p_{i-1,j}^1 & \text{if } i = N \end{cases} \\ &+ \begin{cases} p_{i,j}^2 - p_{i,j-1}^2 & \text{if } 1 < j < N \\ p_{i,j}^2 & \text{if } j = 1 \\ -p_{i,j-1}^2 & \text{if } j = N \end{cases}. \end{aligned}$$

We denote by \mathcal{K} the closed convex set defined by

$$\mathcal{K} = \{S = (S_0, S_1, S_2) \in X \times X \times X \mid \forall (i, j) \in \mathcal{G}, (S_0)_{i,j} \geq \sqrt{(S_1)_{i,j}^2 + (S_2)_{i,j}^2}\}.$$

We now turn to the design of the optimization problem we consider next. It classically comprises a regularization on the unknowns to be recovered, ensuring thus spatial consistency, a data fidelity term, as well as geometrical constraint enforcement. In order to both reconstruct S in compliance with the prescribed physical conditions and induce some coupling between the channels S_1 and S_2 , the discontinuity sets of both S_1 and S_2 being located at the same position, we propose introducing an $S_1 - S_2$ joint total variation regularization denoted by $TV_C(S_1, S_2)$. The underlying goal is to capture a smooth angle of polarization reflecting more faithfully the physical properties of the materials present in the image. It is defined by

$$\begin{aligned} TV_C(S_1, S_2) &= \sum_{(i,j) \in \mathcal{G}} \sqrt{\left((\nabla S_1)_{i,j}^1 \right)^2 + \left((\nabla S_1)_{i,j}^2 \right)^2 + \left((\nabla S_2)_{i,j}^1 \right)^2 + \left((\nabla S_2)_{i,j}^2 \right)^2}. \end{aligned} \tag{5}$$

As a shortened notation, the following will be used:

$$TV_C(\tilde{s}) = TV_C(S_1, S_2) = \sum_{(i,j) \in \mathcal{G}} \|(\nabla \tilde{s})_{i,j}\|_{\mathbb{R}^4}, \tag{6}$$

where $(\nabla \tilde{s})_{i,j} = \left((\nabla S_1)_{i,j}, (\nabla S_2)_{i,j} \right)$. The motivation for introducing such a regularizer is that it favours reconstructions of S_1 and S_2 in which contours are at the same location, owing to the simple observation that $\sqrt{a^2 + b^2} \leq \sqrt{a^2} + \sqrt{b^2}$ (refer to [21] for further details). The joint $S_1 - S_2$ total variation is complemented by a standard total variation smoother on S_0 denoted by

$$\begin{aligned} TV(S_0) &= \sum_{(i,j) \in \mathcal{G}} \sqrt{\left((\nabla S_0)_{i,j}^1 \right)^2 + \left((\nabla S_0)_{i,j}^2 \right)^2} \\ &= \sum_{(i,j) \in \mathcal{G}} \|(\nabla S_0)_{i,j}\|_{\mathbb{R}^2}, \end{aligned}$$

a fidelity term $\mathcal{F} = \mathcal{F}(S)$ defined by

$$\mathcal{F}(S) = \frac{\mu}{2} \sum_{(i,j) \in \mathcal{G}} \|AS_{i,j} - I_{i,j}\|_{\mathbb{R}^4}^2,$$

and prescribed geometrical conditions, yielding the following constrained optimization problem:

$$\inf_{S \in \mathcal{K}} \mathcal{J}(S) = TV_C(S_1, S_2) + TV(S_0) + \mathcal{F}(S). \tag{P}$$

A first theoretical result ensures the existence/uniqueness of the minimizer of problem (P).

Theorem 1 *Problem (P) admits a unique solution.*

Proof The set \mathcal{K} is closed and convex, while the objective function is continuous and coercive. Indeed, $\forall(i, j) \in \mathcal{G}$, one has:

$$\begin{aligned} \frac{\mu}{2} \|AS_{i,j} - I_{i,j}\|_{\mathbb{R}^4}^2 &\geq \frac{\mu}{4} \|AS_{i,j}\|_{\mathbb{R}^4}^2 - \frac{\mu}{2} \|I_{i,j}\|_{\mathbb{R}^4}^2 \\ &\geq \frac{\mu}{4} \left(((S_0)_{i,j})^2 + \frac{1}{2} ((S_1)_{i,j})^2 + \frac{1}{2} ((S_2)_{i,j})^2 \right) \\ &\quad - \frac{\mu}{2} \|I_{i,j}\|_{\mathbb{R}^4}^2, \end{aligned}$$

(since $A^T A = \begin{pmatrix} 1 & 0 & 0 \\ 0 & \frac{1}{2} & 0 \\ 0 & 0 & \frac{1}{2} \end{pmatrix}$), so that

$$\begin{aligned} \mathcal{J}(S) &\geq \frac{\mu}{8} \left(\|S_0\|_X^2 + \|S_1\|_X^2 + \|S_2\|_X^2 \right) \\ &\quad - \frac{\mu}{2} \sum_{(i,j) \in \mathcal{G}} \|I_{i,j}\|_{\mathbb{R}^4}^2, \end{aligned}$$

or equivalently,

$$\mathcal{J}(S) \geq \frac{\mu}{8} \|S\|_{X^3}^2 - \frac{\mu}{2} \|I\|_{X^4}^2,$$

with the classical Euclidean norms and their standard notation. The related scalar products will be denoted by $\langle \cdot, \cdot \rangle$, without necessarily specifying the current dimension as index.

In addition, the functional is strictly convex, which yields the desired result. \square

To lighten the notations, when there is no ambiguity about the dimension of the mathematical objects we handle, we omit the lower indices in the definition of the Euclidean norms.

3.2 Reformulation as a Min–Max Problem

Motivated by prior related works by Chambolle and Pock [14] dedicated to primal-dual algorithms, we now restate our optimization problem as a min–max one, using the dual formulation of the introduced coupled total variation.

Functional TV_C is positively homogeneous of degree one since $\forall \tilde{s} \in X \times X, \forall \lambda > 0, TV_C(\lambda \tilde{s}) = \lambda TV_C(\tilde{s})$, so that its Legendre–Fenchel transform [22] TV_C^* defined by

$$TV_C^*(\tilde{t}) = \sup_{\tilde{s} \in X \times X} \langle \tilde{s}, \tilde{t} \rangle - TV_C(\tilde{s})$$

is the indicator function of a closed convex set \mathcal{A} :

$$TV_C^*(\tilde{t}) = \begin{cases} 0 & \text{if } \tilde{t} \in \mathcal{A} \\ +\infty & \text{otherwise} \end{cases}.$$

Since $TV_C^{**} = TV_C$, it readily comes that

$$TV_C(\tilde{s}) = \sup_{\tilde{t} \in \mathcal{A}} \langle \tilde{s}, \tilde{t} \rangle.$$

It remains to make the set \mathcal{A} explicit. Going back to the basic definition of $TV_C(\tilde{s})$ (5)–(6), clearly, $\forall \tilde{s} \in X \times X$,

$$\begin{aligned} TV_C(\tilde{s}) &= \sup_{p=(p_1,p_2) \in Y \times Y} \langle \nabla \tilde{s}, p \rangle \\ &= \sup_{p=(p_1,p_2) \in Y \times Y} \langle \nabla S_1, p_1 \rangle_Y + \langle \nabla S_2, p_2 \rangle_Y, \end{aligned}$$

with the supremum taken over $p \in Y \times Y$ such that $\forall(i, j) \in \mathcal{G}$,

$$\|p_{i,j}\|_{\mathbb{R}^4} = \sqrt{((p_1)_{i,j}^1)^2 + ((p_1)_{i,j}^2)^2 + ((p_2)_{i,j}^1)^2 + ((p_2)_{i,j}^2)^2} \leq 1.$$

Using the discrete divergence operator introduced earlier, we get:

$$\begin{aligned} \langle \nabla S_1, p_1 \rangle_Y + \langle \nabla S_2, p_2 \rangle_Y \\ = -\langle S_1, \text{div } p_1 \rangle_X - \langle S_2, \text{div } p_2 \rangle_X, \end{aligned}$$

yielding

$$\begin{aligned} \mathcal{A} &= \{ \text{div } p = \begin{pmatrix} \text{div } p_1 \\ \text{div } p_2 \end{pmatrix} \text{ with } p \in Y \times Y \mid \\ &\quad \forall(i, j) \in \mathcal{G}, \|p_{i,j}\|_{\mathbb{R}^4} \leq 1 \}. \end{aligned}$$

With this material and in particular the dual formulation of the classical total variation (see [20]), we are now able to rephrase our optimization problem as a min–max one.

$$\begin{aligned} \inf_{S=(S_0,S_1,S_2) \in \mathcal{K}} \sup_{p=(p_0,p_1,p_2) \in \mathcal{B}} \mathcal{L}(S, p) & \tag{P̄} \\ := \langle \nabla S, p \rangle + \frac{\mu}{2} \sum_{(i,j) \in \mathcal{G}} \|AS_{i,j} - I_{i,j}\|_{\mathbb{R}^4}^2, \end{aligned}$$

with

$$\langle \nabla S, p \rangle = \langle \nabla S_0, p_0 \rangle_Y + \langle \nabla S_1, p_1 \rangle_Y + \langle \nabla S_2, p_2 \rangle_Y,$$

and \mathcal{B} being the convex set defined by

$$\begin{aligned} \mathcal{B} &= \{ p = (p_0, p_1, p_2) = (p_0, \tilde{p}) \\ &\quad \in Y \times Y \times Y \mid \forall(i, j) \in \mathcal{G}, \|\tilde{p}_{i,j}\|_{\mathbb{R}^4} \\ &\quad \leq 1 \text{ and } \|(p_0)_{i,j}\|_{\mathbb{R}^2} \leq 1 \}. \end{aligned}$$

A first result ensures that the Lagrangian \mathcal{L} possesses a saddle point. Before stating this theoretical result, we recall some basic facts on duality by the minimax theorem mostly taken

from [23, Chapter VI]. We use the same notations as Ekeland and Témam and consider the general minimization problem phrased as

$$\inf_{u \in V} \Phi(u) \tag{7}$$

and termed *primal problem*. We assume that $\Phi(u)$ can be rewritten as a supremum in p of a function $L(u, p)$ as

$$\inf_{u \in V} \sup_{p \in Z} L(u, p). \tag{8}$$

A related problem named *dual of (7)* is defined by

$$\sup_{p \in Z} \inf_{u \in V} L(u, p). \tag{9}$$

A natural question is to ask about the link between problems (8) and (9).

The sets \mathcal{A} and \mathcal{B} being arbitrary for the moment, a first result states that if L is a function on $\mathcal{A} \times \mathcal{B}$ with real values, one always has

$$\sup_{p \in \mathcal{B}} \inf_{u \in \mathcal{A}} L(u, p) \leq \inf_{u \in \mathcal{A}} \sup_{p \in \mathcal{B}} L(u, p).$$

Let us now recall the definition of a saddle point.

Definition 1 Taken from [23, Chapter VI, Definition 1.1] We say that a pair $(\bar{u}, \bar{p}) \in \mathcal{A} \times \mathcal{B}$ is a saddle point of L on $\mathcal{A} \times \mathcal{B}$ if, $\forall u \in \mathcal{A}, \forall p \in \mathcal{B}$,

$$L(\bar{u}, p) \leq L(\bar{u}, \bar{p}) \leq L(u, \bar{p}).$$

Proposition 1 Taken from [23, Chapter VI, Proposition 1.2] *The function L defined on $\mathcal{A} \times \mathcal{B}$ with real values possesses a saddle point (\bar{u}, \bar{p}) on $\mathcal{A} \times \mathcal{B}$ if and only if*

$$\max_{p \in \mathcal{B}} \inf_{u \in \mathcal{A}} L(u, p) = \min_{u \in \mathcal{A}} \sup_{p \in \mathcal{B}} L(u, p),$$

and this number is then equal to $L(\bar{u}, \bar{p})$.

Now, to legitimize the introduction of our min–max algorithm, it remains to establish the connection between a saddle point of L and a minimizer of the primal problem (7).

In that purpose, let us assume that (\bar{u}, \bar{p}) is a saddle point of L . From the left-hand side of the inequality in Definition 1., one gets :

$$\inf_{u \in \mathcal{A}} \Phi(u) \leq \Phi(\bar{u}) = \sup_{p \in \mathcal{B}} L(\bar{u}, p) \leq L(\bar{u}, \bar{p}).$$

Now, from the right-hand side of the inequality in Definition 1., it comes

$$L(\bar{u}, \bar{p}) \leq \inf_{u \in \mathcal{A}} L(u, \bar{p}).$$

But $\forall u \in \mathcal{A}, L(u, \bar{p}) \leq \sup_{p \in \mathcal{B}} L(u, p)$, yielding $\inf_{u \in \mathcal{A}} L(u, \bar{p}) \leq \inf_{u \in \mathcal{A}} \sup_{p \in \mathcal{B}} L(u, p) = \inf_{u \in \mathcal{A}} \Phi(u)$. Consequently, if (\bar{u}, \bar{p}) is a saddle point of L , then \bar{u} is a minimizer of Φ .

Before stating the main theoretical result, we recall a criterion that will be useful in the proof.

Proposition 2 Taken from [23, Chapter VI, Proposition 1.3] *If there exists $u_0 \in \mathcal{A}, p_0 \in \mathcal{B}$ and $\alpha \in \mathbb{R}$ such that*

$$\forall p \in \mathcal{B}, L(u_0, p) \leq \alpha,$$

$$\forall u \in \mathcal{A}, L(u, p_0) \geq \alpha,$$

then (u_0, p_0) is a saddle point of L and

$$\alpha = \inf_{u \in \mathcal{A}} \sup_{p \in \mathcal{B}} L(u, p) = \sup_{p \in \mathcal{B}} \inf_{u \in \mathcal{A}} L(u, p).$$

Equipped with this material, we are now ready to state the main theoretical result.

Theorem 2 *The Lagrangian \mathcal{L} of problem $(\bar{\mathcal{P}})$ possesses at least one saddle point (\bar{S}, \bar{p}) on $\mathcal{K} \times \mathcal{B}$.*

The proof is an adaptation of the one of [23, Chapter VI, Proposition 2.1] in which the sets \mathcal{A} and \mathcal{B} are assumed to be bounded, which is not the case in our problem. We adopt some of the notations of [23, Chapter VI, Proposition 2.1].

Proof For every $p \in \mathcal{B}, S \mapsto \mathcal{L}(S, p)$ is strictly convex, owing to the strict convexity of functional \mathcal{F} . For each $p \in \mathcal{B}$, functional $S \mapsto \mathcal{L}(S, p)$ is continuous and coercive. To establish such a coercivity inequality, denoting by $\kappa = \|\text{div}\| = \sup_{\|p\|_{Y^3} \leq 1} \|\text{div } p\|_{X^3}$, we first observe that with the convention $(p_0)_{0,j}^1 = (p_0)_{N,j}^1 = (p_0)_{i,0}^2 = (p_0)_{i,N}^2 = 0$ (similarly for p_1 and p_2) and by applying twice the inequality $(a + b)^2 \leq 2(a^2 + b^2)$,

$$\begin{aligned} & \|\text{div } p\|_{X^3}^2 \\ &= \sum_{(i,j) \in \mathcal{G}} [((p_0)_{i,j}^1 - (p_0)_{i-1,j}^1 + (p_0)_{i,j}^2 - (p_0)_{i,j-1}^2)^2 \\ &+ ((p_1)_{i,j}^1 - (p_1)_{i-1,j}^1 + (p_1)_{i,j}^2 - (p_1)_{i,j-1}^2)^2 \\ &+ ((p_2)_{i,j}^1 - (p_2)_{i-1,j}^1 + (p_2)_{i,j}^2 - (p_2)_{i,j-1}^2)^2] \\ &\leq 4 \sum_{(i,j) \in \mathcal{G}} [((p_0)_{i,j}^1)^2 + ((p_0)_{i-1,j}^1)^2 + ((p_0)_{i,j}^2)^2 + ((p_0)_{i,j-1}^2)^2] \\ &+ 4 \sum_{(i,j) \in \mathcal{G}} [((p_1)_{i,j}^1)^2 + ((p_1)_{i-1,j}^1)^2 + ((p_1)_{i,j}^2)^2 + ((p_1)_{i,j-1}^2)^2] \\ &+ 4 \sum_{(i,j) \in \mathcal{G}} [((p_2)_{i,j}^1)^2 + ((p_2)_{i-1,j}^1)^2 + ((p_2)_{i,j}^2)^2 + ((p_2)_{i,j-1}^2)^2] \\ &\leq 8 \|p_0\|_Y^2 + 8 \|p_1\|_Y^2 + 8 \|p_2\|_Y^2 = 8 \|p\|_{Y^3}^2. \end{aligned}$$

Thus, $\kappa \leq 2\sqrt{2}$ and

$$\begin{aligned} \mathcal{L}(S, p) &\geq \frac{\mu}{8} \|S\|_{X^3}^2 - \|\operatorname{div}\| \|p\|_{Y^3} \|S\|_{X^3} - \frac{\mu}{2} \|I\|_{X^4}^2 \\ &\geq \frac{\mu}{8} \|S\|_{X^3}^2 - 4N \|S\|_{X^3} - \frac{\mu}{2} \|I\|_{X^4}^2, \end{aligned}$$

since $p \in \mathcal{B}$, entailing that $\|p\|_{Y^3}^2 \leq 2N^2$. Now, using Young’s inequality with ϵ (valid for every $\epsilon > 0$) and stated by $ab \leq \frac{a^2}{2\epsilon} + \frac{\epsilon b^2}{2}$,

$$\mathcal{L}(S, p) \geq \left(\frac{\mu}{8} - \frac{\epsilon}{2}\right) \|S\|_{X^3}^2 - \frac{8N^2}{\epsilon} - \frac{\mu}{2} \|I\|_{X^4}^2.$$

This latter inequality shows that by choosing ϵ sufficiently small, the coercivity property is ensured. $\forall p \in \mathcal{B}$, $\mathcal{L}(S, p)$ is bounded below independently of p and one remarks that $\forall p \in \mathcal{B}$, $\mathcal{L}(0, p) = \frac{\mu}{2} \|I\|_{X^4}^2$ so that the infimum is finite. Then, for each $p \in \mathcal{B}$, functional $\mathcal{L}(\cdot, p)$ is continuous, coercive and strictly convex so it admits a unique minimizer in \mathcal{K} denoted by $e(p)$. We denote this minimum by $f(p)$, i.e.

$$f(p) = \min_{S \in \mathcal{K}} \mathcal{L}(S, p) = \mathcal{L}(e(p), p). \tag{10}$$

Function $p \mapsto f(p)$ is concave as the pointwise infimum of concave functions ($\forall S \in \mathcal{K}$, $p \mapsto \mathcal{L}(S, p)$ is concave). This is a standard result of analysis that we nevertheless recall in Appendix A. for the sake of completeness. Also, f is upper semi-continuous as the pointwise infimum of continuous functions ($\forall S \in \mathcal{K}$, $p \mapsto \mathcal{L}(S, p)$ is continuous). Again, this is a standard result of analysis for which we provide a proof in Appendix B. It is therefore bounded above and attains its upper bound as the set \mathcal{B} is compact, at a point denoted by \bar{p} . Thus,

$$f(\bar{p}) = \max_{p \in \mathcal{B}} f(p) = \max_{p \in \mathcal{B}} \min_{S \in \mathcal{K}} \mathcal{L}(S, p).$$

Additionally, as $f(\bar{p}) = \min_{S \in \mathcal{K}} \mathcal{L}(S, \bar{p})$, one has

$$\forall S \in \mathcal{K}, f(\bar{p}) \leq \mathcal{L}(S, \bar{p}). \tag{11}$$

By concavity of \mathcal{L} with respect to the second argument (even linearity), $\forall S \in \mathcal{K}$, $\forall p \in \mathcal{B}$ and $\forall \lambda \in]0, 1[$, $\mathcal{L}(S, (1 - \lambda)\bar{p} + \lambda p) \geq (1 - \lambda)\mathcal{L}(S, \bar{p}) + \lambda \mathcal{L}(S, p)$. Taking as particular value $S = e_\lambda = e((1 - \lambda)\bar{p} + \lambda p)$, it yields, using again that $f(\bar{p}) = \max_{p \in \mathcal{B}} f(p)$ and the concavity of \mathcal{L} with respect to the second argument,

$$\begin{aligned} f(\bar{p}) &\geq f((1 - \lambda)\bar{p} + \lambda p) = \mathcal{L}(e_\lambda, (1 - \lambda)\bar{p} + \lambda p) \\ &\geq (1 - \lambda)\mathcal{L}(e_\lambda, \bar{p}) + \lambda \mathcal{L}(e_\lambda, p). \end{aligned}$$

As $\mathcal{L}(e_\lambda, \bar{p}) \geq f(\bar{p}) = \min_{S \in \mathcal{K}} \mathcal{L}(S, \bar{p})$, the latter inequality implies that $\forall p \in \mathcal{B}$,

$$f(\bar{p}) \geq \mathcal{L}(e_\lambda, p). \tag{12}$$

By virtue of the coercivity property established previously and the fact that $\forall p \in \mathcal{B}$, $\mathcal{L}(0, p) = \frac{\mu}{2} \|I\|_{X^4}^2$, one has $\forall p \in \mathcal{B}$, (parameter $\epsilon > 0$ being sufficiently small so that $\frac{\mu}{8} - \frac{\epsilon}{2} > 0$),

$$\begin{aligned} &\left(\frac{\mu}{8} - \frac{\epsilon}{2}\right) \|e_\lambda\|_{X^3}^2 - \frac{8N^2}{\epsilon} - \frac{\mu}{2} \|I\|_{X^4}^2 \\ &\leq \mathcal{L}(e_\lambda, (1 - \lambda)\bar{p} + \lambda p) \leq \frac{\mu}{2} \|I\|_{X^4}^2, \end{aligned}$$

showing that e_λ is uniformly bounded. One can thus extract a subsequence e_{λ_n} with $\lambda_n \xrightarrow{n \rightarrow +\infty} 0$ converging to some limit \bar{S} . We show next that $\bar{S} = e(\bar{p})$. In particular, \bar{S} depends neither on p , nor on the selected sequence λ_n . As by definition $\mathcal{L}(e_\lambda, (1 - \lambda)\bar{p} + \lambda p) = \min_{S \in \mathcal{K}} \mathcal{L}(S, (1 - \lambda)\bar{p} + \lambda p)$, $\forall S \in \mathcal{K}$,

$$\mathcal{L}(e_\lambda, (1 - \lambda)\bar{p} + \lambda p) \leq \mathcal{L}(S, (1 - \lambda)\bar{p} + \lambda p),$$

and by concavity of \mathcal{L} with respect to the second argument, it follows that $\forall S \in \mathcal{K}$,

$$(1 - \lambda)\mathcal{L}(e_\lambda, \bar{p}) + \lambda \mathcal{L}(e_\lambda, p) \leq \mathcal{L}(S, (1 - \lambda)\bar{p} + \lambda p).$$

The quantity $\mathcal{L}(e_\lambda, p)$ is bounded below by $f(p)$ so that passing to the limit in the previous inequality when λ_n tends to 0 yields, using the continuity of \mathcal{L} ,

$$\mathcal{L}(\bar{S}, \bar{p}) \leq \mathcal{L}(S, \bar{p}),$$

this being true for all $S \in \mathcal{K}$. By uniqueness of the minimizer of problem $\min_{S \in \mathcal{K}} \mathcal{L}(S, \bar{p})$, we deduce that $\bar{S} = e(\bar{p})$.

At last, passing to the limit in (12) yields $\mathcal{L}(\bar{S}, p) \leq f(\bar{p})$, $\forall p \in \mathcal{B}$, which combines with (11) and the invocation of Proposition 2. enables one to conclude that (\bar{S}, \bar{p}) is a saddle point of \mathcal{L} . \square

4 Numerical Algorithm

Our problem (\bar{P}) falls within the general framework of convex optimization problems with known saddle-point structure addressed in [14] and for which the authors provide a resolution algorithm with guaranteed convergence. Before making this connection more explicit, we review some preliminary mathematical results devoted to convex optimization. The dimension N is considered next for purposes of illustration, but the results can of course be extended/adapted to other dimensions.

4.1 Preliminary Mathematical Background

We denote by \mathbb{R}^N the usual N -dimensional Euclidean space and by $\|\cdot\|$ its norm, while I refers to the identity matrix.

The domain of a function $f : \mathbb{R}^N \rightarrow]-\infty, +\infty]$ is denoted by $\text{dom } f$ and defined by $\text{dom } f = \{x \in \mathbb{R}^N \mid f(x) < +\infty\}$.

The notation $\Gamma_0(\mathbb{R}^N)$ refers to the set of lower-semicontinuous convex functions from \mathbb{R}^N to $]-\infty, +\infty]$ such that $\text{dom } f \neq \emptyset$.

The subdifferential of f is the set-valued operator

$$\partial f : \mathbb{R}^N \rightarrow 2^{\mathbb{R}^N} : x \mapsto \{u \in \mathbb{R}^N \mid \forall y \in \mathbb{R}^N, f(y) \geq f(x) + (y - x)^T u\}.$$

Let C be a nonempty subset of \mathbb{R}^N . The indicator function of C is such that:

$$i_C : x \mapsto \begin{cases} 0 & \text{if } x \in C \\ +\infty & \text{if } x \notin C \end{cases}.$$

The distance from $x \in \mathbb{R}^N$ to C is defined by $d_C(x) = \inf_{y \in C} \|x - y\|$. If the set C is closed and convex, the projection of $x \in \mathbb{R}^N$ onto C is the unique point $P_C x \in C$ such that $d_C(x) = \|x - P_C x\|$.

The projection $P_C x$ of $x \in \mathbb{R}^N$ onto the nonempty closed convex set $C \subset \mathbb{R}^N$ can be viewed as the solution of the problem

$$\min_{y \in \mathbb{R}^N} i_C(y) + \frac{1}{2} \|x - y\|^2,$$

function i_C being an element of $\Gamma_0(\mathbb{R}^N)$ due to the assumptions on C .

This formulation led Moreau [24] to extend the notion of projection wherein an arbitrary function $f \in \Gamma_0(\mathbb{R}^N)$ is now a substitute for i_C . This yields the definition of the so-called proximal or proximity operator.

Definition 2 Proximal/Proximity operator (Taken from [25, Definition 10.1]) Let $f \in \Gamma_0(\mathbb{R}^N)$. For every $x \in \mathbb{R}^N$, the minimization problem

$$\min_{y \in \mathbb{R}^N} f(y) + \frac{1}{2} \|x - y\|^2$$

admits a unique solution denoted by $\text{prox}_f(x)$. The operator $\text{prox}_f : \mathbb{R}^N \rightarrow \mathbb{R}^N$ thus defined is the proximal operator of f .

The proximal operator exhibits suitable properties. With $f \in \Gamma_0(\mathbb{R}^N)$, it is characterized by:

$$\forall (x, p) \in \mathbb{R}^N \times \mathbb{R}, p = \text{prox}_f(x) \iff x - p \in \partial f(p).$$

It enjoys another fine property well-suited for iterative minimization algorithms: it is firmly nonexpansive and its fixed point set is precisely the set of minimizers of f , which dictates the way proximal operator-based algorithms are designed.

4.2 The Generic Chambolle–Pock Primal-dual Algorithm

Equipped with this material, we now relate our problem with the general framework developed in [14] and see how the primal-dual algorithm presented therein can be adapted to our case. As made explicit in Sect. 4.3, problem (\mathcal{P}) falls within the generic saddle-point problem addressed in [14] and phrased as

$$\min_{x \in X} \max_{y \in Y} \langle Kx, y \rangle + G(x) - F^*(y), \tag{13}$$

X and Y being two finite-dimensional real vector spaces equipped with an inner product $\langle \cdot, \cdot \rangle$ and norm $\|\cdot\| = \langle \cdot, \cdot \rangle^{\frac{1}{2}}$, $K : X \rightarrow Y$ being a continuous linear operator with induced norm

$$\|K\| = \max \{\|Kx\| \mid x \in X \text{ with } \|x\| \leq 1\},$$

G and F^* being proper, convex, lower semi-continuous (lsc), and F^* being itself the convex conjugate of a convex lsc function F . Then, the general given algorithm in [14] reads as:

Algorithm 1 General Chambolle–Pock primal-dual algorithm ([14, Algorithm 1.])

- 1: Initialization: Choose $\tau, \sigma > 0, \theta \in [0, 1], (x^0, y^0) \in X \times Y$ and set $\bar{x}^0 = x^0$.
 - 2: **for** $n = 0, 1, \dots$ **do**
 - 3: $y^{n+1} = \text{prox}_{\sigma F^*}(y^n + \sigma K \bar{x}^n)$;
 - 4: $x^{n+1} = \text{prox}_{\tau G}(x^n - \tau K^* y^{n+1})$;
 - 5: $\bar{x}^{n+1} = x^{n+1} + \theta (x^{n+1} - x^n)$.
 - 6: **end for**
-

Remark 1 It can be easily observed that fixed points of Algorithm 1 are saddle points of the associated Lagrangian. Indeed, if one considers a fixed point (x^*, y^*) of the algorithm, owing to the fact that

$$\begin{aligned} r = \text{prox}_f(s) &\iff s - r \in \partial f(r) \\ &\iff \forall t, f(t) \geq f(r) + \langle s - r, t - r \rangle, \end{aligned}$$

the first relation $y^* = \text{prox}_{\sigma F^*}(y^* + \sigma K x^*)$ of the algorithm gives

$$\begin{aligned} \forall y \in Y, \sigma F^*(y) &\geq \sigma F^*(y^*) + \langle y - y^*, \sigma K x^* \rangle \\ \iff \forall y \in Y, -F^*(y) + \langle y, K x^* \rangle &\leq -F^*(y^*) + \langle y^*, K x^* \rangle, \end{aligned} \tag{14}$$

while the second relation $x^* = \text{prox}_{\tau G}(x^* - \tau K^* y^*)$ yields

$$\begin{aligned} \forall x \in X, \tau G(x) &\geq \tau G(x^*) - \langle \tau K^* y^*, x - x^* \rangle \\ \iff \forall x \in X, G(x) &\geq G(x^*) - \langle K^* y^*, x - x^* \rangle \\ \iff \forall x \in X, G(x^*) + \langle K^* y^*, x^* \rangle &\leq G(x) + \langle K^* y^*, x \rangle. \end{aligned} \tag{15}$$

Summing (14) and (15) leads to

$$\begin{aligned} \forall x \in X, \forall y \in Y, \langle K x^*, y \rangle + G(x^*) - F^*(y) \\ \leq \langle K x, y^* \rangle + G(x) - F^*(y^*), \end{aligned}$$

showing that (x^*, y^*) is a saddle point of the associated Lagrangian.

Remark 2 A convergence result is established in [14, Theorem 1] with $\theta = 1$ and provided that $\tau\sigma\|K\|^2 < 1$.

4.3 Design of our Numerical Algorithm

Our problem is a special instance of (13) with $K = \nabla, F^* = i_{\mathcal{B}}$ and $G(S) = i_{\mathcal{K}}(S) + \frac{\mu}{2} \sum_{(i,j) \in \mathcal{G}} \|AS_{i,j} - I_{i,j}\|_{\mathbb{R}^4}^2$ and can be rephrased as

$$\begin{aligned} \min_{S=(S_0, S_1, S_2) \in X^3} \max_{p=(p_0, p_1, p_2) \in Y^3} \\ \langle \nabla S, p \rangle + i_{\mathcal{K}}(S) + \frac{\mu}{2} \sum_{(i,j) \in \mathcal{G}} \|AS_{i,j} - I_{i,j}\|_{\mathbb{R}^4}^2 - i_{\mathcal{B}}(p). \end{aligned} \tag{P}$$

Thus, the first step of the algorithm 1. reads as

$$p^{n+1} = \text{prox}_{\sigma i_{\mathcal{B}}}(p^n + \sigma \nabla \bar{S}^n),$$

which amounts to computing the projection of $p^n + \sigma \nabla \bar{S}^n$ onto the closed convex set \mathcal{B} denoted by $P_{\mathcal{B}}(p^n + \sigma \nabla \bar{S}^n)$. More precisely, given $z = (z_0, z_1, z_2) \in Y^3 = (z_0, \tilde{z}) \in Y \times Y^2, \forall (i, j) \in \mathcal{G}$,

$$(P_{\mathcal{B}}(z))_{i,j} = \left(\frac{(z_0)_{i,j}}{\max(1, \|(z_0)_{i,j}\|_{\mathbb{R}^2})}, \frac{\tilde{z}_{i,j}}{\max(1, \|\tilde{z}_{i,j}\|_{\mathbb{R}^4})} \right).$$

The second step of the algorithm reads as

$$S^{n+1} = \text{prox}_{\tau G}(S^n + \tau \text{div } p^{n+1}),$$

or equivalently,

$$\begin{aligned} S^{n+1} = \arg \min_{\tilde{S} \in X^3} \frac{1}{2} \|\tilde{S} - (S^n + \tau \text{div } p^{n+1})\|_{X^3}^2 + i_{\mathcal{K}}(\tilde{S}) \\ + \frac{\tau\mu}{2} \sum_{(i,j) \in \mathcal{G}} \|A\tilde{S}_{i,j} - I_{i,j}\|_{\mathbb{R}^4}^2. \end{aligned}$$

We observe that the problem is separable with respect to each $\tilde{S}_{i,j}$ so that

$$\text{prox}_{\tau G}(w) = \left(\text{prox}_{\tau g_{i,j}}(w_{i,j}) \right)_{(i,j) \in \mathcal{G}},$$

w being an element of $X^3, g_{i,j}$ being defined by $g_{i,j} : \mathbb{R}^3 \ni u = (u_0, u_1, u_2) \mapsto i_{\hat{\mathcal{C}}}(u) + \frac{\mu}{2} \|A u - I_{i,j}\|_{\mathbb{R}^4}^2$ with $\hat{\mathcal{C}} = \left\{ t = (t_0, t_1, t_2) \in \mathbb{R}^3 \mid t_0 \geq \sqrt{t_1^2 + t_2^2} \right\}$, which leads us to focus on the single three-dimensional subproblem

$$\begin{aligned} u^* = \arg \min_{\tilde{u} \in \mathbb{R}^3} \frac{1}{2\tau} \|\tilde{u} - u\|_{\mathbb{R}^3}^2 + \frac{\mu}{2} \|A\tilde{u} - I\|_{\mathbb{R}^4}^2 + i_{\hat{\mathcal{C}}}(\tilde{u}) \\ = \text{prox}_{\tau g}(u) = \arg \min_{\tilde{u} \in \mathbb{R}^3} l(\tilde{u}) + i_{\hat{\mathcal{C}}}(\tilde{u}), \end{aligned} \tag{16}$$

(for the sake of generalization, the indices (i, j) on g and I have been removed and I is now a vector of \mathbb{R}^4). Additionally, we denote by $\mathbb{R}^3 \ni b = (b_0, b_1, b_2)^T = \begin{pmatrix} b_0 \\ \bar{b} \end{pmatrix} = A^T I$ and

by h the function $h : t = (t_0, t_1, t_2) \in \mathbb{R}^3 \mapsto \sqrt{t_1^2 + t_2^2} - t_0$.

According to [22, Chapter V, Theorem V.8.] (Kuhn-Tucker theorem), u^* is a solution of (16) if and only if there exists $\lambda \in \mathbb{R}^+$ such that

$$\begin{cases} 0 \in \partial l(u^*) + \lambda \partial h(u^*) \\ \lambda h(u^*) = 0. \end{cases} \tag{17}$$

Due to the separability property $h(t) = h_0(t_0) + h_1(t_1, t_2)$, one has

$$\begin{aligned} \partial h(t) = (\partial h_0(t_0), \partial h_1(\bar{t} = (t_1, t_2))) \\ = \{v = (v_0, \bar{v} = (v_1, v_2)) \in \mathbb{R} \times \mathbb{R}^2 \mid v_0 \\ \in \partial h_0(t_0), \bar{v} \in \partial h_1(\bar{t})\}. \end{aligned}$$

The inclusion $(\partial h_0(t_0), \partial h_1(\bar{t})) \subset \partial h(t)$ is straightforward. Suppose that $(v_0, \bar{v}) \in \partial h_0(t_0) \times \partial h_1(\bar{t})$. Then, by definition of the subdifferential, $\forall u = (u_0, u_1, u_2) = (u_0, \bar{u}) \in \mathbb{R}^3$,

$$\begin{cases} h_0(u_0) \geq h_0(t_0) + (u_0 - t_0)v_0, \\ h_1(\bar{u}) \geq h_1(\bar{t}) + \langle \bar{u} - \bar{t}, \bar{v} \rangle. \end{cases}$$

Summing the two previous inequalities yields, $\forall u \in \mathbb{R}^3$

$$h(u) \geq h(t) + \langle u - t, v \rangle,$$

hence $v \in \partial h(t)$.

To prove the converse inclusion $\partial h(t) \subset (\partial h_0(t_0), \partial h_1(\bar{t}))$, we argue by contradiction and consider $v \in \partial h(t)$ such that $v \notin (\partial h_0(t_0), \partial h_1(\bar{t}))$. Without loss of generality, we may assume that $\bar{v} \notin \partial h_1(\bar{t})$ (the reasoning being the same if $v_0 \notin \partial h_0(t_0)$ is assumed). Consequently, there exists $\bar{u} \in \mathbb{R}^2$ such that

$$h_1(\bar{u}) < h_1(\bar{t}) + \langle \bar{u} - \bar{t}, \bar{v} \rangle.$$

Let us now take $u = (u_0, \bar{u})$ with \bar{u} defined as above and $u_0 = t_0$. Then

$$\begin{aligned} h(u) &= h_0(u_0) + h_1(\bar{u}) < h_0(t_0) + h_1(\bar{t}) + \langle u - t, v \rangle \\ &= h(t) + \langle u - t, v \rangle, \end{aligned}$$

which contradicts the fact that $v \in \partial h(t)$. In the end,

$$\begin{aligned} \partial h(t) &= (\partial h_0(t_0), \partial h_1(\bar{t})) = \left(-1, \partial_{\|\cdot\|_{\mathbb{R}^2}}(\bar{t})\right) \\ &= \left(-1, \begin{cases} \frac{\bar{t}}{\|\bar{t}\|_{\mathbb{R}^2}} & \text{if } \bar{t} \neq 0_{\mathbb{R}^2} \\ \{a \in \mathbb{R}^2 \mid \|a\|_{\mathbb{R}^2} \leq 1\} & \text{if } \bar{t} = 0_{\mathbb{R}^2} \end{cases}\right). \end{aligned}$$

We now go back to the necessary and sufficient conditions (17). These now read as $(u^* = (u_0^*, u_1^*, u_2^*) = (u_0^*, \bar{u}^*))$

$$\begin{cases} \left(\frac{1}{\tau} + \mu\right) u_0^* - \frac{1}{\tau} u_0 - \mu b_0 - \lambda = 0, \\ \left(\frac{1}{\tau} + \frac{\mu}{2}\right) \bar{u}^* - \frac{1}{\tau} \bar{u} - \mu \bar{b} + \lambda \partial_{\|\cdot\|_{\mathbb{R}^2}}(\bar{u}^*) \ni 0, \\ \lambda (\|\bar{u}^*\|_{\mathbb{R}^2} - u_0^*) = 0. \end{cases} \tag{18}$$

Setting $z_0 = \frac{\frac{1}{\tau} u_0 + \mu b_0}{\alpha}$ and $\bar{z} = \frac{\frac{1}{\tau} \bar{u} + \mu \bar{b}}{\beta}$ with $\alpha = \frac{1}{\tau} + \mu$ and $\beta = \frac{1}{\tau} + \frac{\mu}{2}$, these conditions amount to

$$\begin{cases} u_0^* = z_0 + \frac{\lambda}{\alpha}, \\ \bar{u}^* - \bar{z} + \frac{\lambda}{\beta} \partial_{\|\cdot\|_{\mathbb{R}^2}}(\bar{u}^*) \ni 0, \\ \lambda (\|\bar{u}^*\|_{\mathbb{R}^2} - u_0^*) = 0. \end{cases} \tag{19}$$

We distinguish two cases:

- **Case for which $\lambda = 0$:** Then $\begin{cases} u_0^* = z_0 \\ \bar{u}^* = \bar{z} \end{cases}$, with $z_0 \geq \|\bar{z}\|_{\mathbb{R}^2}$.
- **Case for which $\lambda > 0$:**

- **Subcase $z_0 \geq 0$:** $u_0^* = \|\bar{u}^*\|_{\mathbb{R}^2}$. $u_0^* \neq 0$ otherwise λ would be negative. Thus, $\bar{u}^* \neq 0_{\mathbb{R}^2}$ so that the second KKT condition in (19) reads $\bar{u}^* + \frac{\lambda}{\beta} \frac{\bar{u}^*}{\|\bar{u}^*\|_{\mathbb{R}^2}} = \bar{z}$ expressing the fact that \bar{u}^* and \bar{z} are colinear with a positive coefficient. Straightforward computations give $\bar{u}^* = \left(1 - \frac{\lambda}{\beta \|\bar{z}\|_{\mathbb{R}^2}}\right) \bar{z}$ with $\lambda < \beta \|\bar{z}\|_{\mathbb{R}^2}$. At last, the first condition of (19) combined with the slackness condition (third equation of (19)) leads to

$$\lambda = \frac{\alpha\beta}{\alpha + \beta} (\|\bar{z}\|_{\mathbb{R}^2} - z_0)$$

with $z_0 < \|\bar{z}\|_{\mathbb{R}^2}$ ($\lambda < \beta \|\bar{z}\|_{\mathbb{R}^2}$ is ensured). Thus,

$$\begin{cases} u_0^* = \frac{\alpha}{\alpha + \beta} z_0 + \frac{\beta}{\alpha + \beta} \|\bar{z}\|_{\mathbb{R}^2}, \\ \bar{u}^* = \left(\frac{\beta}{\alpha + \beta} + \frac{\alpha}{\alpha + \beta} \frac{z_0}{\|\bar{z}\|_{\mathbb{R}^2}}\right) \bar{z}. \end{cases}$$

- **Subcase $z_0 < 0$:** $u_0^* = \|\bar{u}^*\|_{\mathbb{R}^2}$. If $\bar{u}^* = 0_{\mathbb{R}^2}$, then $u_0^* = 0$ and $\lambda = -\alpha z_0$. The second KKT condition in (19) gives $\beta \|\bar{z}\|_{\mathbb{R}^2} \leq -\alpha z_0$. If $\bar{u}^* \neq 0_{\mathbb{R}^2}$, again the second KKT condition in (19) shows that \bar{u}^* and \bar{z} are colinear with positive coefficient $\left(1 - \frac{\lambda}{\beta \|\bar{z}\|_{\mathbb{R}^2}}\right)$ so $\lambda < \beta \|\bar{z}\|_{\mathbb{R}^2}$. The first condition of (19) combined with the slackness condition (third equation of (19)) leads to

$$\lambda = \frac{\alpha\beta}{\alpha + \beta} (\|\bar{z}\|_{\mathbb{R}^2} - z_0)$$

($\lambda > 0$ is automatically satisfied), the constraint $\lambda < \beta \|\bar{z}\|_{\mathbb{R}^2}$ reads equivalently $\beta \|\bar{z}\|_{\mathbb{R}^2} > -\alpha z_0$ and in the end,

$$\begin{cases} u_0^* = \frac{\alpha}{\alpha + \beta} z_0 + \frac{\beta}{\alpha + \beta} \|\bar{z}\|_{\mathbb{R}^2}, \\ \bar{u}^* = \left(\frac{\beta}{\alpha + \beta} + \frac{\alpha}{\alpha + \beta} \frac{z_0}{\|\bar{z}\|_{\mathbb{R}^2}}\right) \bar{z}. \end{cases}$$

To summarize, it can be checked that:

- If $z_0 \geq 0$
 - If $\|\bar{z}\|_{\mathbb{R}^2} \leq z_0$, $\text{prox}_{\tau g}(u) = (z_0, \bar{z})$;
 - If $\|\bar{z}\|_{\mathbb{R}^2} > z_0$,

$$\begin{aligned} \text{prox}_{\tau g}(u) &= \left(\frac{\alpha}{\alpha + \beta} z_0 \right. \\ &\quad \left. + \frac{\beta}{\alpha + \beta} \|\bar{z}\|_{\mathbb{R}^2}, \left(\frac{\beta}{\alpha + \beta} + \frac{\alpha}{\alpha + \beta} \frac{z_0}{\|\bar{z}\|_{\mathbb{R}^2}}\right) \bar{z}\right); \end{aligned}$$

- If $z_0 < 0$

- (i) If $\beta \|\bar{z}\|_{\mathbb{R}^2} \leq -\alpha z_0$, $\text{prox}_{\tau g}(u) = (0, 0_{\mathbb{R}^2})$;
- (ii) If $\beta \|\bar{z}\|_{\mathbb{R}^2} > -\alpha z_0$,

$$\text{prox}_{\tau g}(u) = \left(\frac{\alpha}{\alpha + \beta} z_0 + \frac{\beta}{\alpha + \beta} \|\bar{z}\|_{\mathbb{R}^2}, \left(\frac{\beta}{\alpha + \beta} + \frac{\alpha}{\alpha + \beta} \frac{z_0}{\|\bar{z}\|_{\mathbb{R}^2}} \right) \bar{z} \right).$$

Remark 3 An alternative technique based on the orthogonal projection onto epigraphs can be provided to obtain the expression of $\text{prox}_{\tau g}(u)$. This can be found in Appendix C.

According to Remark 2, convergence is ensured if $\theta = 1$ and $\tau\sigma\|\nabla\|^2 < 1$. Since $\|\text{div}\| = \|\nabla\|$ ([26, Chapter IV, Sect. 5, Theorem 6]) and due to the previous estimate on $\|\text{div}\|$, convergence is thus guaranteed as soon as $\tau\sigma < \frac{1}{8}$.

5 Validation

5.1 Experimental Results

To achieve the validation of the proposed theory on real Stokes images, experiments are conducted on intensity images acquired from a polarimetric camera. Note that the data that support the findings of this study are not openly available but are available from the corresponding author upon reasonable request. In our experiments, the trioptics polar4D camera is used, providing four images I_0, I_{45}, I_{90} and I_{135} . The Stokes images are calculated both with the classical least square method (LS) and with the proposed one. The question of assessing the validity of the proposed model over the classical least square-based one encompasses several levels of discussion. Indeed, the presented experiments are intended to quantify both the relevancy of the regularization and the compliance of the recovered Stokes vectors with the physical admissibility criterion as well as sensitivity to noise. To achieve this goal and in addition to visual inspection, two metrics that encode those aspects are assessed: on the one hand, the monitoring of the DOLP for the physical admissibility verification, and on the other hand, the control of the AOLP for the physical consistency of the scene. As previously stressed, the DOLP lies between zero and one, whilst the AOLP should be homogeneous on objects made of the same material. The Stokes images calculated with the least square method as usually done in the literature are compared to those computed using the proposed solution. More precisely, to demonstrate the validity/relevance of the regularization and its influence on the AOLP over the classical least square method (LS), three configurations are considered when relevant: (i) the pure geometrical model without regularization named Geometrical Model Alone (GMA) in which the TV regularization has been removed, thus consisting of

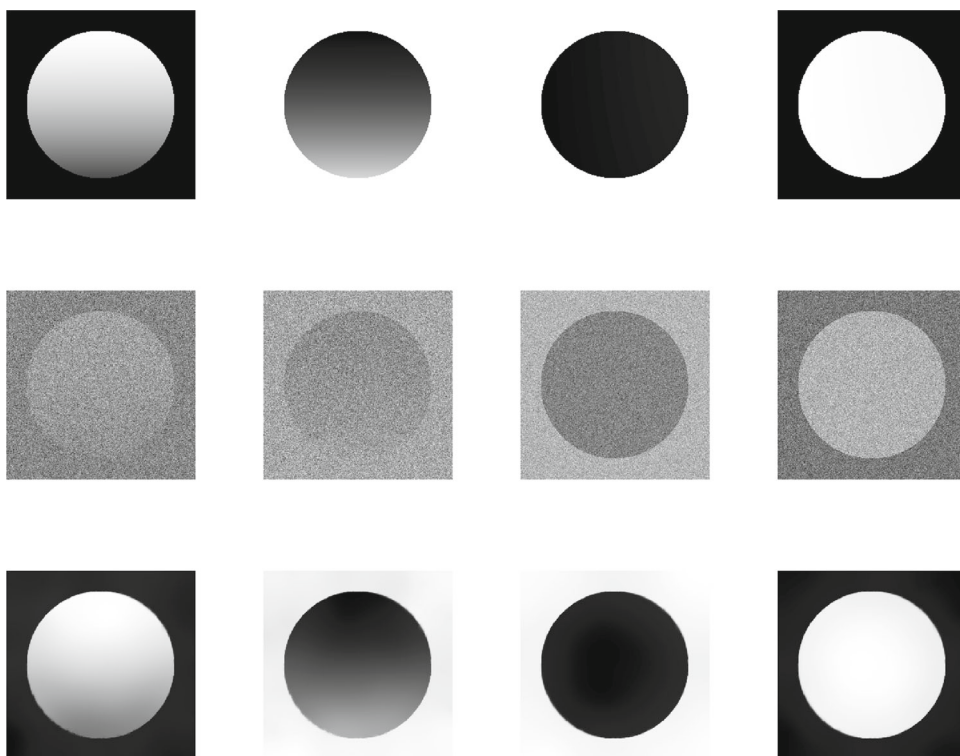
the classical L^2 -penalization coupled with the geometrical constraints, (ii) the model with decoupled regularization on each channel referred to as Decoupled Model (DM) in which total variation regularization is applied independently on each channel, and (iii) our Coupled Model (CM). By saying ‘when relevant’, we mean when LS produces DOLP values strictly greater than 1, otherwise we restrict ourselves to a mere comparison between LS and CM since in this case, the physical admissibility constraints will not be active in GMA.

Extensive experiments conducted to discriminate between DM and CM show the preeminence of CM over DM, both in terms of quantitative criteria such as the AOLP and DOLP, and qualitative assessment (spatial regularization/coherency, more refined details). Thus in the presentation, we limit ourselves to the comparisons of the LS method, GMA and CM, the latter model being the one detailed in the paper. The best solution is the one achieving a DOLP between 0 and 1, while exhibiting a piecewise homogeneous AOLP. The first condition related to the DOLP ($S_0 \geq \sqrt{S_1^2 + S_2^2}$) reflects the fact that the total energy of the light wave S_0^2 is always greater than the energy of the deterministic part of that wave, $S_1^2 + S_2^2$, whereas the condition on AOLP translates the fact that two spatially close identical objects should mainly reflect the light in the same direction. The experiments are split into two sets of images: simple indoor images containing object/background and real outdoor images with non-controlled light.

5.1.1 Experiments on Synthetic Data and Indoor Images

In order to substantiate the relevancy of the proposed approach, simulations on synthetic data for which ground truth is known have been performed. The artificial data have been generated based on an earlier code by Dr. Sylvain Faisan (ICube - MIV, Université de Strasbourg) dedicated to the reconstruction of full Stokes vectors [10] and that we adapted to our setting. We synthesized a 256×256 pixel Stokes image $S^{st} = [S_0^{st}, S_1^{st}, S_2^{st}]$ composed of two distinct regions: (i) a background with a uniform polarization signature $S^{st} = [1, \frac{1}{\sqrt{2}}, \frac{1}{\sqrt{2}}]$ (totally polarized light), and (ii) a circle of radius 100 pixels with a smoothly varying partially polarized Stokes signature. The associated radiance images $I^{st} = [I_0^{st}, I_{90}^{st}, I_{45}^{st}, I_{135}^{st}]$ are computed ($I^{st} = AS^{st}$) and are then degraded by an additive white Gaussian noise of variance $\sigma^2 = 0.02$. These are depicted in Fig. 3 (both clean radiance images and degraded counterparts). The initial set of data is shown in Fig. 3 second row, while the reconstructed Stokes vectors are displayed in Fig. 4 second row, the tuning parameters being set, respectively, to $\sigma = 0.3$ (Chambolle–Pock algorithm), $\gamma = 1, \theta = 0.5$ and $\mu = 1.5$. Visually, the reconstruction is smooth and spatially consistent, emphasizing the benefit of total variation regularization and obeys the

Fig. 3 First row: synthetic clean radiance images, from left to right I_0^{gt} , I_{90}^{gt} , I_{45}^{gt} , I_{135}^{gt} . Second row: their counterpart degraded by a white additive Gaussian noise with $\sigma^2 = 0.02$. Third row: recovered radiance images I^* obtained by computing AS^* . The PSNR between the noise-free radiance images I^{gt} and the estimated ones I^* is 37.36



admissibility constraint criterion, the DOLP being an element of $[0, 1]$ (see Fig. 5). As the ground truth is known, these elements can be corroborated by the accuracy assessment, by comparing the estimated values S^* with the original ones S^{gt} through the formula (see again [10])

$$\mathcal{E}(S^{gt}, S^*) = 100 \sqrt{\frac{1}{P} \sum_x \frac{\|S^{gt}(x) - S^*(x)\|^2}{\|S^{gt}(x)\|^2}},$$

with P the number of pixels and $\|\cdot\|$ denoting the Euclidean norm in \mathbb{R}^3 . In our experiment, the Stokes vector estimation error is $\mathcal{E}(S^{gt}, S^*) = 2.79$. Note that if the Total Variation regularization proves to be relevant in removing noise while preserving sharp edges, one of its limitations is the contrast loss (see [27]). To circumvent this issue in future works, several lines of research could be considered among which: sequential pipelines with a posteriori contrast enhancement while still preserving the physical admissibility constraint (histogram equalization, gray-scale transformation algorithms, PDE-based methods, etc.) or joint frameworks including new fidelity terms.

In a second configuration, experiments are conducted on real indoor images with a few objects on a unified background. In order to avoid strong reflections focused on areas where the light source is shining, acquisitions are carried out under uniform illumination, during the day and without any artificial illumination. The protocol is illustrated on an acquisition example in Fig. 6.

The objective of this first cohort of experiments is to demonstrate, on simple object images, the quality of the recovered AOLP without any parasitic incident illumination as well as the homogeneity of the Stokes components. The media of the pot as well as the plant are not reflective, which avoids any disturbing specular reflection. Figure 7 displays the three polarization channels S_0 , S_1 and S_2 of a plant in its pot obtained, respectively, with CM constrained by $\sigma = 0.1$ (Chambolle–Pock algorithm), $\gamma = 1$, $\theta = 0.5$ and $\mu = 20$, LS and GMA, while Fig. 8 depicts the AOLP and DOLP metrics in each case. Components S_1 and S_2 produced by CM are smoother than those obtained with LS and GMA, highlighting the benefit of TV regularization whilst preserving significant information. As for the DOLP, although visually similar, the ranges are not the same and in particular, the DOLP exceeds 1 at some pixels with the LS method. Those pixels having a $DOLP > 1$ are not physically admissible. In comparison, the DOLP calculated with the proposed method, with or without (CM/GMA) regularization, is always between 0 and 1 for each pixel, due to the exact geometrical constraint enforcement. It is worth reminding the reader that the non-compliance of some pixels with the physical constraint leads gradually to an erroneous reflection from the pixel and then to an irrelevant estimation of the object surface properties represented by the corresponding Stokes vectors. In that case, there is even no guarantee that the estimated Stokes vectors of pixels fulfilling the physical admissibility criterion are pertinent. This way of calculating

Fig. 4 First row: ground truth Stokes vector $S^{gt} = [S_0^{gt}, S_1^{gt}, S_2^{gt}]$. Second row: estimated Stokes vector S^*

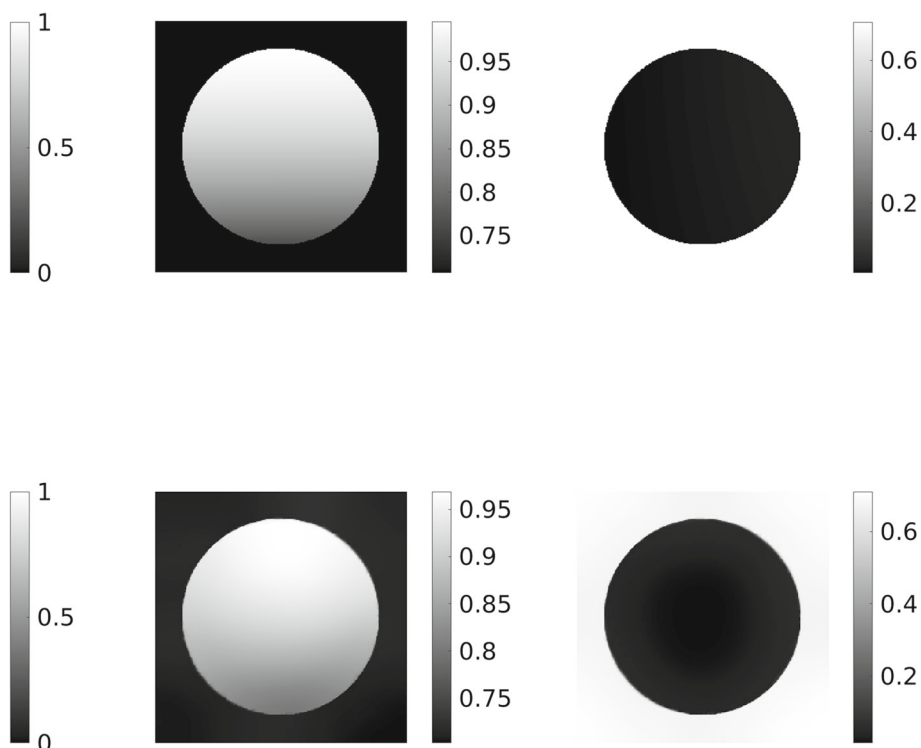
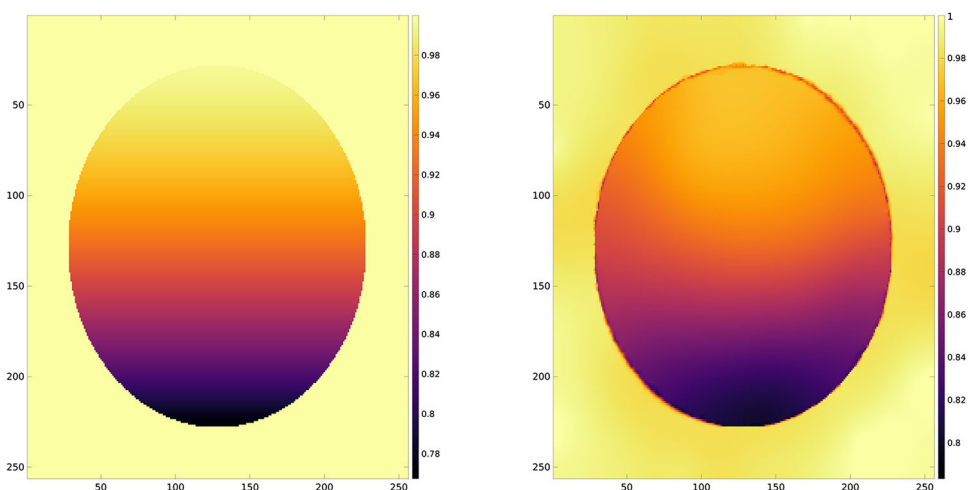


Fig. 5 Left: ground truth DOLP computed from S^{gt} . Right: DOLP computed from the estimated Stokes vector S^*



the Stokes vectors is potentially wrong, showing the superiority of the proposed solution that not only respects the physical constraints of the polarization formalism but ensures homogeneity of the AOLP as will be seen next.

The second metric that has been considered here is the AOLP. When the classical least square-based method is applied, the AOLP seems to be corrupted by randomly distributed points, whereas it should be comparable for an object made of the same material. This issue is always present in the AOLP estimation and is, most of the time, a direct consequence of the non-compliance of some pixels with the

physical admissibility constraint, even if it affects only a few of them. The AOLP is better represented with the proposed CM model. In this case, the AOLP is smoother, more homogeneous for an area made of the same material, especially in the regions where the incident light is uniform.

In order to substantiate even better the interest of the proposed model that handles both the issue of physical admissibility and spatial consistency, the acquired raw images from the polarimetric camera are degraded by an additive white Gaussian noise of zero mean and with variance $\sigma^2 = 0.25$. Without loss of generality and to evaluate the sensitivity of



Fig. 6 The experimental protocol

the LS method, this perturbation is applied only on one of the intensity channels arbitrarily chosen to be I_{45} in that case, that is then normalized between 0 and 1. These are displayed in Fig. 9, while the reconstructed Stokes components S_0 , S_1 , S_2 with CM constrained by $\sigma = 0.3$ (Chambolle–Pock algo-

rithm), $\gamma = 1$, $\theta = 0.5$ and $\mu = 4$ are depicted in Fig. 10, jointly with those obtained by LS and GMA.

The DOLP and AOLP are illustrated in Fig. 11 for each method. Table 1 lists the DOLP mean of the noise-free images and the one of the degraded images, together with the respective standard deviations to measure the amount of dispersion. The different figure contents correlated with the table elements express clearly the relevance of the proposed method to preserve the admissibility of polarimetric images even in noisy acquisitions and in rendering a smooth AOLP map. Moreover, when considering the DOLP calculated with the three methods, it is clear that CM is the one giving the smoother one, emphasizing the ability of the model to handle data corrupted by noise. Slightly smaller standard deviations are obtained in the case of the CM method (noisy and noise-free frameworks), reflecting a smaller dispersion of the DOLP. The significance of the proposed method is also corroborated by the images of the AOLP. Once again, the AOLP of CM is more homogeneous and is more successful in highlighting the homogeneous reflections when dealing with the same material. This analysis is finally substantiated

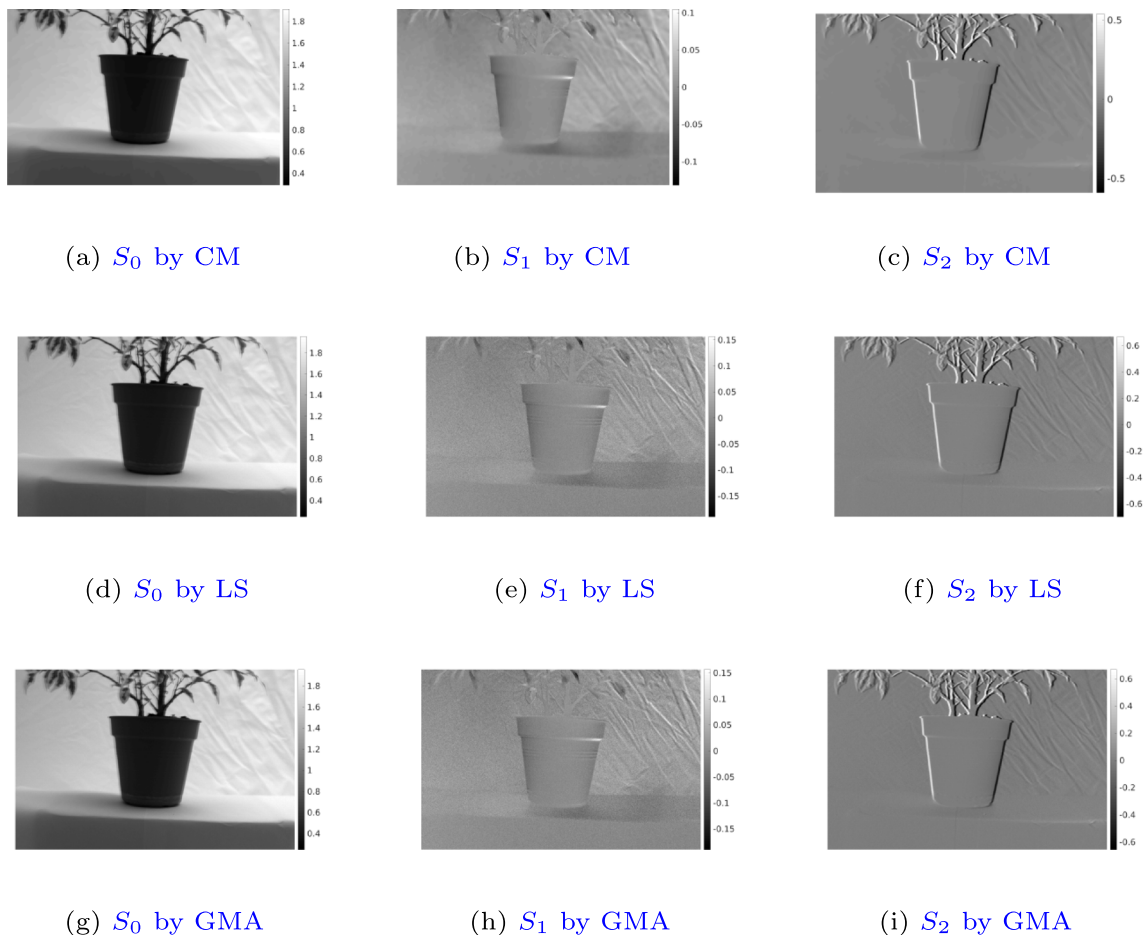


Fig. 7 Row 1: three-dimensional Stokes images S_0 , S_1 , S_2 of a plant in its pot reconstructed with CM. Row 2: three-dimensional Stokes images S_0 , S_1 , S_2 of a plant in its pot reconstructed with LS. Row 3: three-dimensional Stokes images S_0 , S_1 , S_2 of a plant in its pot reconstructed with GMA

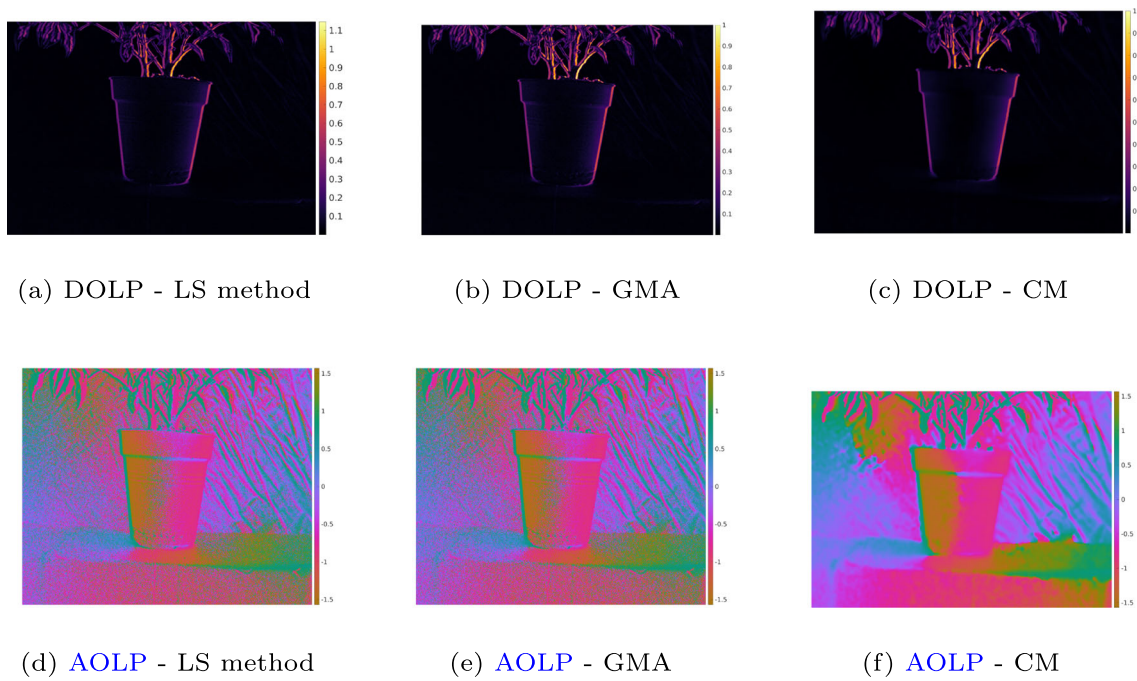


Fig. 8 Row 1: DOLP according to LS method (left), GMA (middle) and CM (right) with colorbar. Row 2: AOLP according to LS method (left), GMA (middle) and CM (right) with colorbar

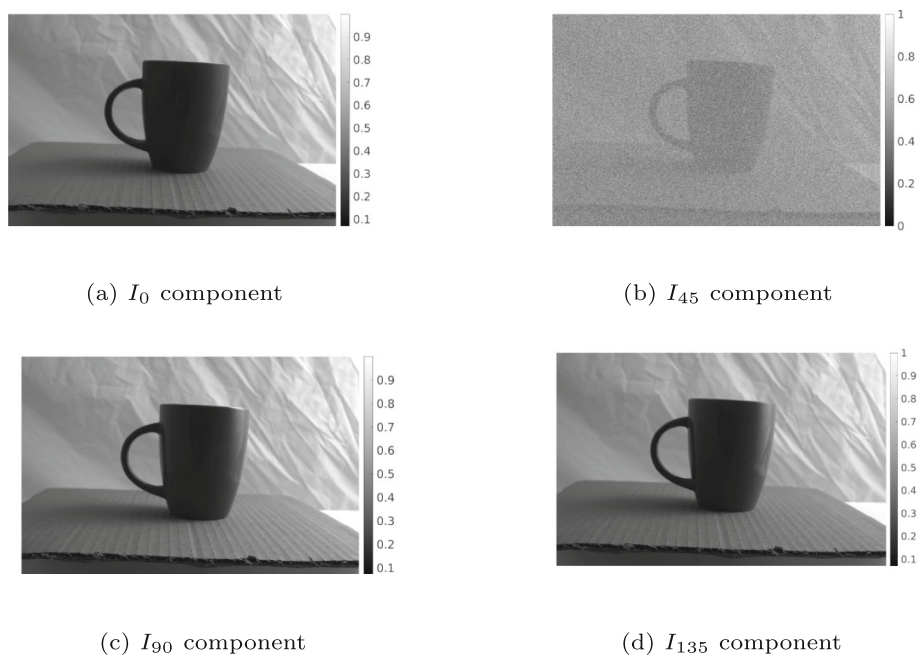


Fig. 9 Corrupted radiance images

by the recovered radiance components $I = AS$ with S the recovered Stokes vectors by CM (Fig. 12), with in particular an estimated I_{45} component that exhibits less noise.

5.1.2 Experiments on Outdoor Polarimetric Images

For the second part of our experiments, the proposed method is evaluated on outdoor scenes with highly reflective objects, uncontrolled heterogeneous incident lights and several objects of different nature. Figure 13 displays the

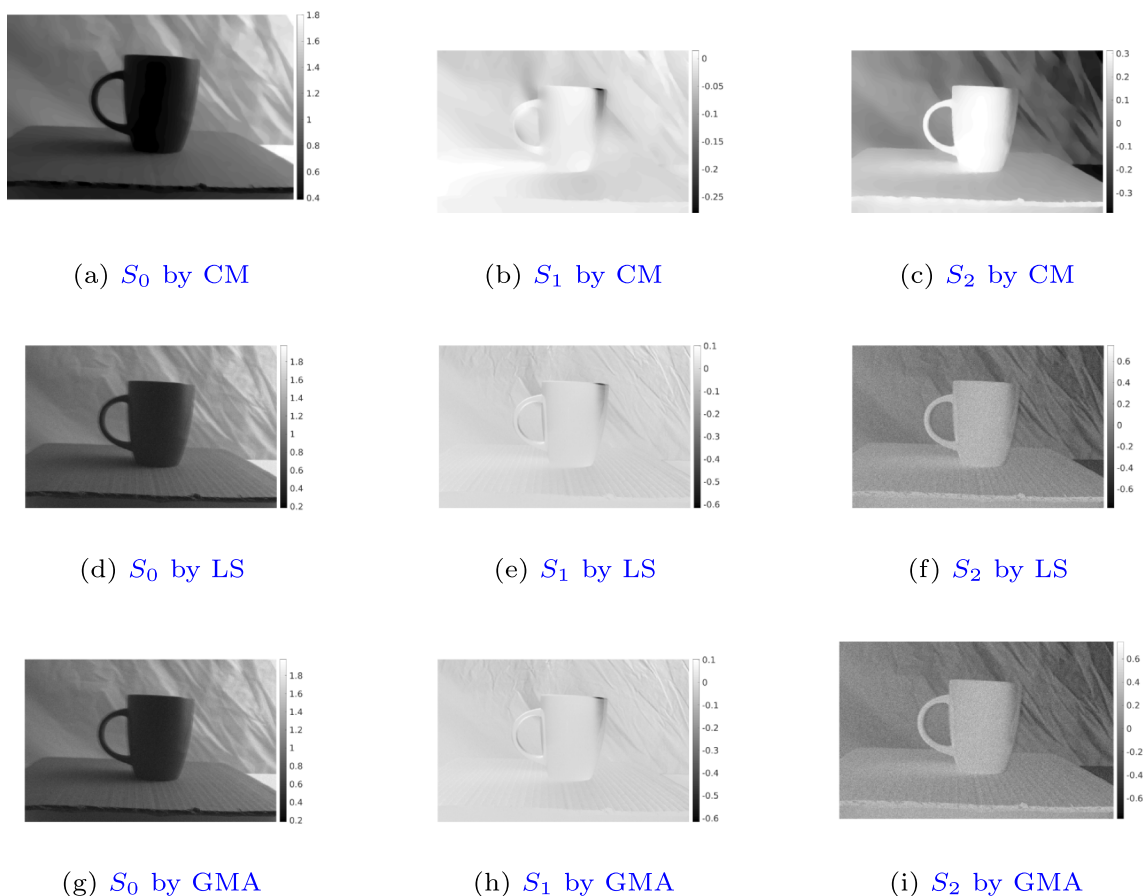


Fig. 10 Row 1: three-dimensional Stokes images S_0 , S_1 , S_2 from corrupted radiance data reconstructed with CM. Row 2: three-dimensional Stokes images S_0 , S_1 , S_2 from corrupted radiance data reconstructed

with LS. Row 3: three-dimensional Stokes images S_0 , S_1 , S_2 from corrupted radiance data reconstructed with GMA

reconstructed Stokes components with CM constrained by $\sigma = 0.1$ (Chambolle–Pock algorithm), $\gamma = 1$, $\theta = 0.5$ and $\mu = 35$, while Fig. 14 emphasizes the results obtained for the DOLP and AOLP with the three methods.

Again, the DOLP with the proposed solution is physically admissible for the whole pixels of the image while for the least square-based model, it is greater than 1 for around 5% of the pixels. As for the AOLP, the proposed method clearly outperforms the classical one, providing a smooth consistent map. For the least square-based method, the map is corrupted by points, meaning that the reflection is strong for these pixels. This phenomenon is physically irrelevant since neighbouring pixels lying on a same material should almost have the same reflection, *i.e.* the same AOLP. As in indoor scenes, this issue occurs because of the non-physical admissibility of the Stokes vectors of some pixels. This problem is amplified for the AOLP estimation. In the coupled regularization model, the AOLP is much better. The reflection in homogeneous areas is roughly the same. Nevertheless, some areas exhibit a high AOLP which indicates a strong reflection:

this occurs in regions where the sun is directly shining. As these areas are localized and not largely spread in the image unlike the least square-based solution, an idea to overcome this problem would be to combine the proposed solution with methods aiming to mitigate specular reflection as presented in [28] or with solutions relying on inpainting to recover the lost part of the AOLP [29]. This is, however, beyond the scope of the proposed work, the problem being independent of the physical admissibility of the Stokes vectors.

The last but not least experiment focuses on complicated outdoor scenes with reduced visibility and poor weather conditions such as heavy fog or snow (see Fig. 15). Recent researches claim that an excellent alternative solution for analysing such complicated images is polarimetric vision, where classical RGB images fail to overcome the drawback of low visibility, resulting in a drop of performances. This can be explained by the fact that an object reflects light even when the visibility is altered. The results of the estimated Stokes vectors with CM constrained by $\sigma = 0.1$ (Chambolle–Pock algorithm), $\gamma = 1$, $\theta = 0.5$ and $\mu = 55$ as well as the

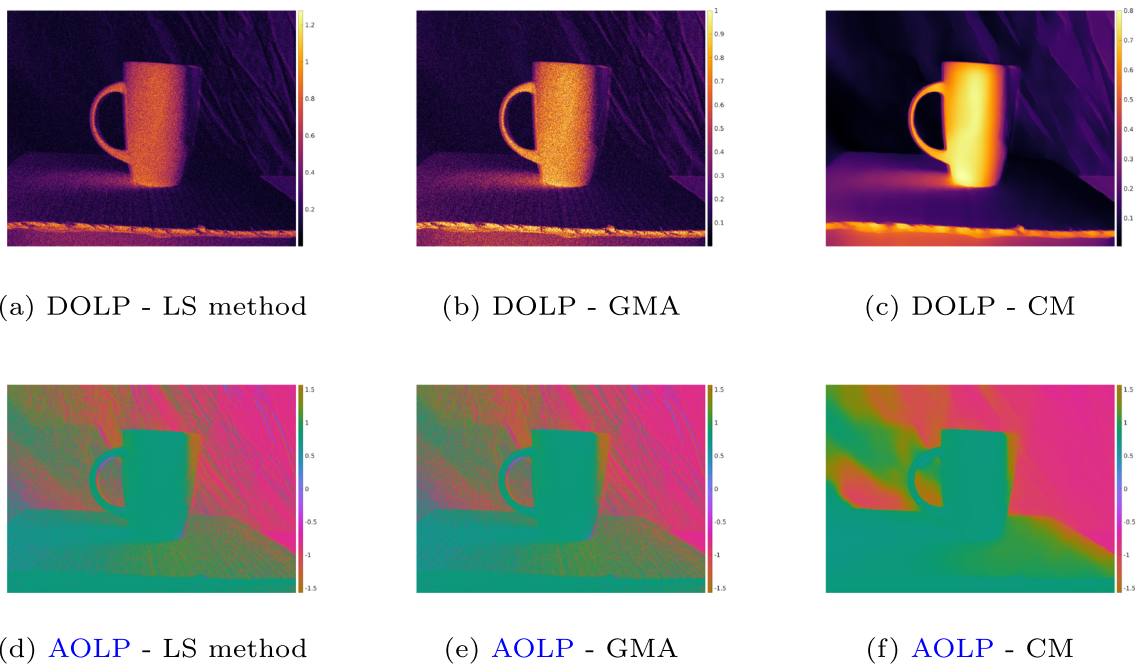
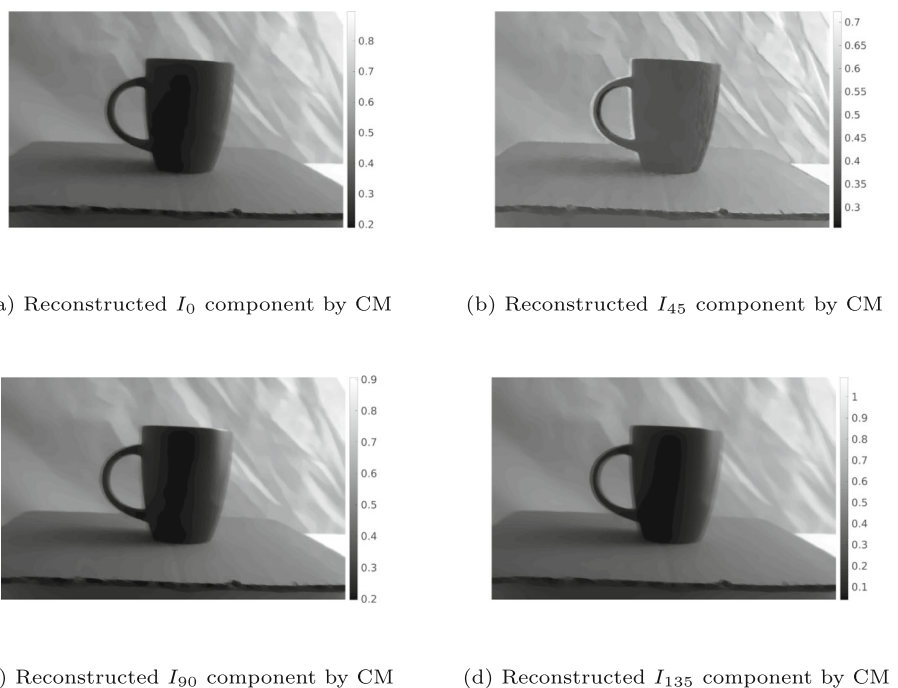


Fig. 11 Row 1: DOLP according to LS method (left), GMA (middle) and CM (right). Row 2: AOLP according to LS method (left), GMA (middle) and CM (right)

Table 1 Comparison of the DOLP mean of noise-free images and noisy images with LS method, GMA and CM: the maximum is in brackets

	LS	GMA	CM
Noise-free images	0.061 ± 0.07 (0.9)	0.061 ± 0.07 (0.9)	0.046 ± 0.051 (0.66)
Noisy images	0.226 ± 0.223 (1.278)	0.225 ± 0.222 (1)	0.202 ± 0.2088 (0.8)

Fig. 12 Reconstructed radiance images by CM



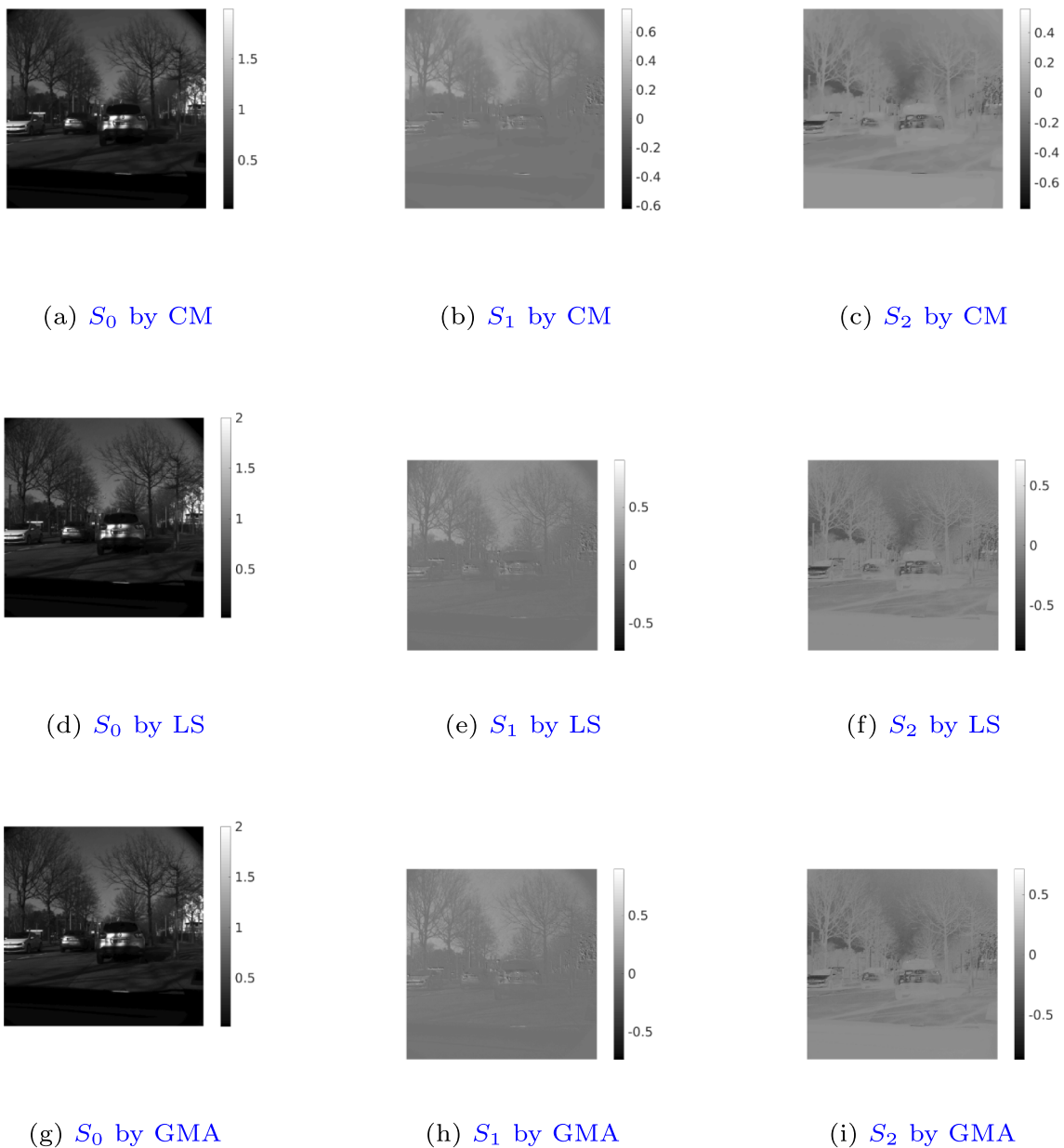


Fig. 13 Row 1: three-dimensional Stokes images S_0 , S_1 , S_2 of an outdoor scene reconstructed with CM. Row 2: three-dimensional Stokes images S_0 , S_1 , S_2 of an outdoor scene reconstructed with LS. Row 3: three-dimensional Stokes images S_0 , S_1 , S_2 of an outdoor scene reconstructed with GMA

polarization characteristics are shown in Figs. 16 and 17, respectively. Note that the LS method produces DOLP values that are lower than 1 so we restrict ourselves to a strict comparison between CM and LS. This experiment thus aims

to support again the fact that coupled TV regularization improves the results. As in all the previous cases, the proposed CM outperforms the classical LS. The AOLP is still not perfect in that case, but one can see much better reflection from distant objects, meaning that the estimated Stokes vectors are more representative of the physical content of the scene (see for instance [30]).

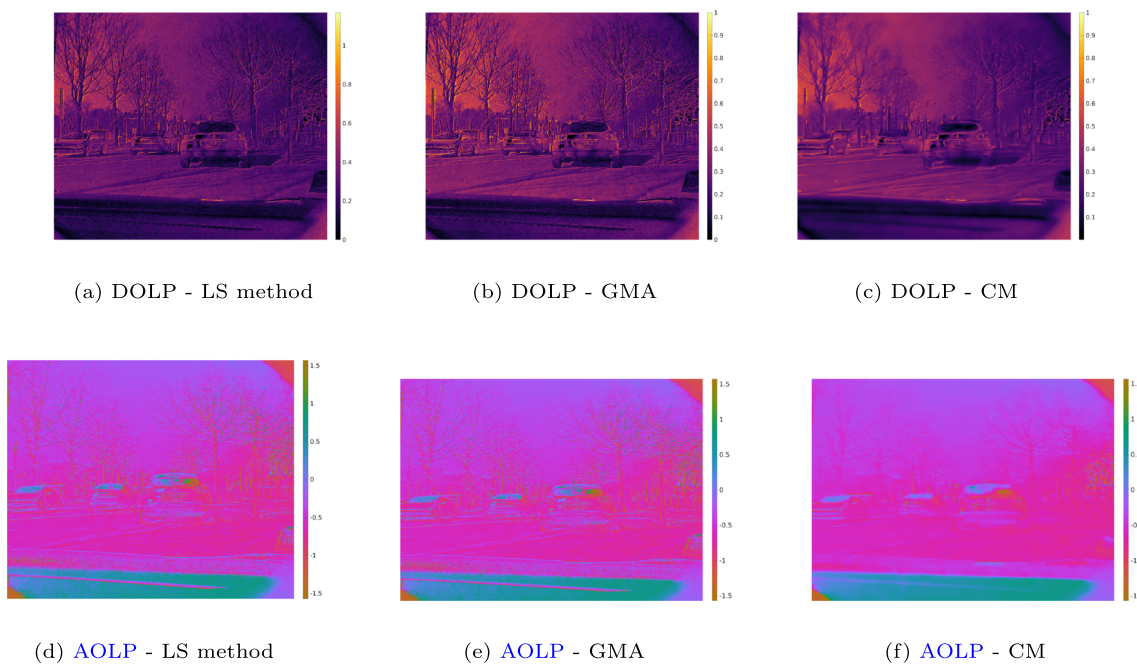


Fig. 14 Row 1: DOLP according to LS method (left), GMA (middle) and CM (right) for the outdoor scene. Row 2: AOLP according to LS method (left), GMA (middle) and CM (right) for the outdoor scene



Fig. 15 Image of a road scene under heavy fog

6 Discussion and Conclusion

This paper shows that a unique solution to the polarization optimization problem can be designed, encoding both the compliance with the physical admissibility constraints and homogeneity/regularity properties, and overcoming thus the limits of the classical least square-based method that is prone to errors. In this latter case, even if these miscalculations might only affect a small amount of pixels, they lead to an

inaccurate physical representation and interpretation of the scene.

Polarization modality is able to characterize an object by multiple physical properties including its intensity, its reflection, its surface nature and roughness, and other induced physical properties such as the DOLP and the AOLP which reflect the magnitude and the direction of the reflection. As most computer vision applications rely on the quantity of information extracted from a scene, it makes polarization modality the best alternative for applications where the classical RGB modality fails. The relevance of the information given by polarization relies first on the correctness of the computed Stokes vectors, crux point of the interpretation of the scene physical content.

We emphasize that the correctness and suitability of the computed Stokes vectors is the primary contribution of our work. Even if the AOLP is still not perfect in the presence of noise, namely in Fig. 11 where noise is deliberately added or in Fig. 17 in the presence of heavy fog and snow, we are nevertheless ensured that, with the proposed solution, the issue does not stem from the non-respect of the physical admissibility constraint, which is essential when dealing with polarization modality. This problem could be addressed in the future by including some pre-processing steps in the pipeline to mitigate the noise affecting acquisitions or to enhance the visibility in the intensity channels before transforming them into Stokes channels. Thus, the restoration phase would be upstream, on the radiance images, and not a posteriori as in the proposed work.. These first

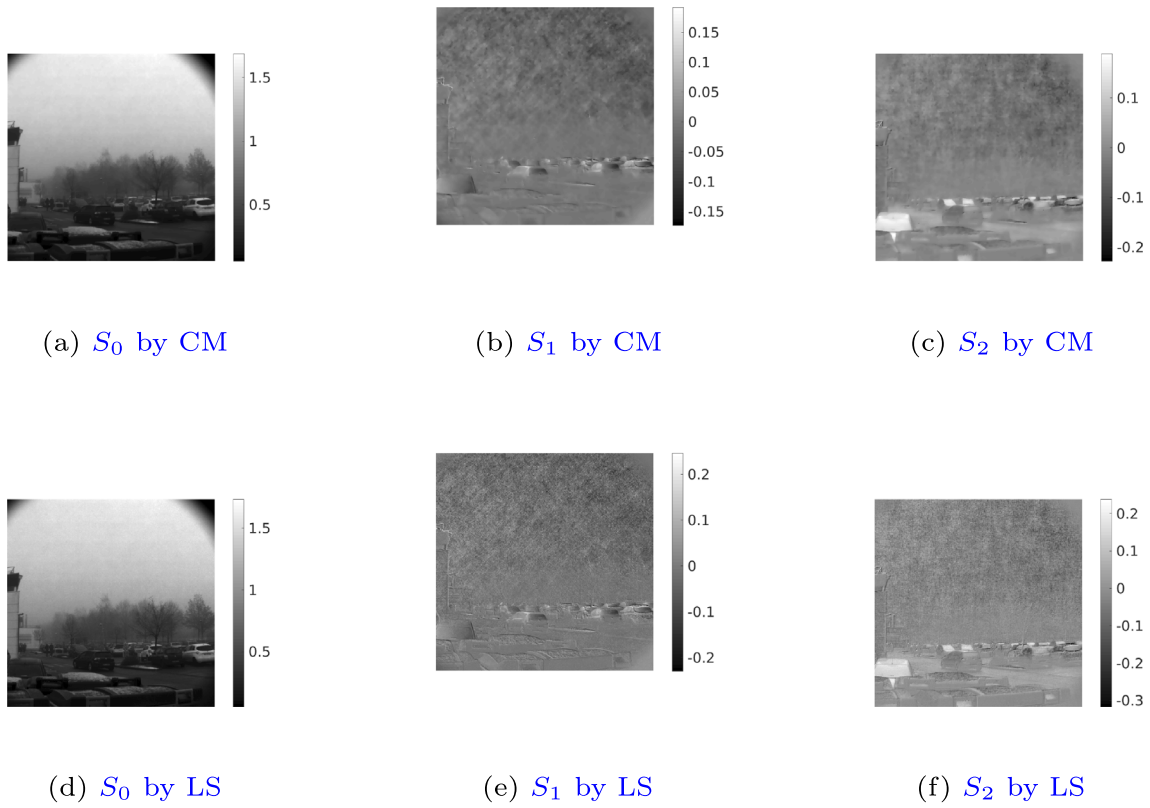
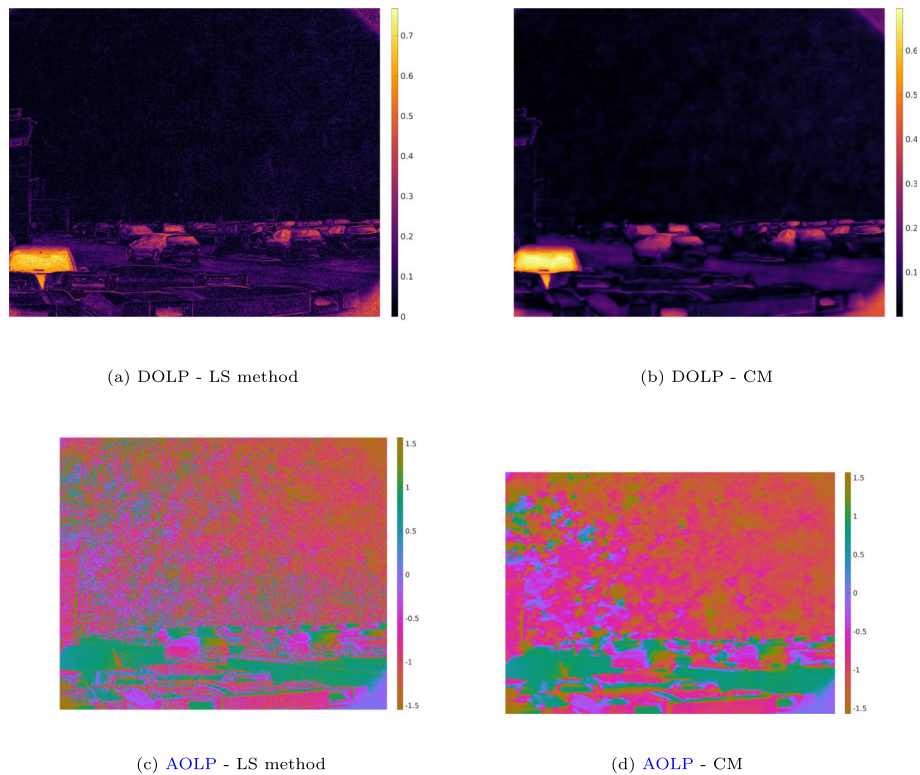


Fig. 16 Row 1: three-dimensional Stokes images S_0, S_1, S_2 of an outdoor scene under heavy fog reconstructed with CM. Row 2: three-dimensional Stokes images S_0, S_1, S_2 of an outdoor scene under heavy fog reconstructed with LS

Fig. 17 Row 1: DOLP according to LS method (left) and CM (right) for the outdoor scene under heavy fog. Row 2: AOLP according to LS method (left) and CM (right) for the outdoor scene under heavy fog



results are cornerstone steps for further processing tasks such as segmentation, classification, detection or more generally, applications requiring a metric or a distance computed directly on Stokes images. So far, for such applications, only the intensity images $(I_0, I_{90}, I_{45}, I_{135})$ have been utilized as complementary information when dealing with polarization-encoded images. Some works, taking advantage of the AOLP and DOLP metrics, are emerging, e.g. shape from polarization [31], transparent object normal estimation [5], showing that this field of research is thriving, enclosing a lot of interesting scientific trails, in particular in computation imaging and graphical display community. Yet, generally, Stokes vectors as well as AOLP and DOLP are most often used to visualize details difficult to see in classical images, such as transparent objects or objects exhibiting specular reflection caused by frontal sunlight. Polarization is also used for scene enhancing, where classical modality fails, such as image dehazing, depth estimation [32,33] or to characterize the dependency of the scene on the illumination conditions [30]. We believe that the proposed work could pave the way to more involved analyses of the Stokes vectors. Indeed, up to now in the literature, no quantitative study entailing the Stokes vectors or a physical combination of them has been introduced. The main reason comes from the mathematical shape of the Stokes vectors: they do not lie in a vector space owing to the physical admissibility constraint. It is therefore inaccurate to use the Euclidean distance to compare pixels represented by two Stokes vectors. Also, two spatially close pixels may lie on different materials. The problem of comparing Stokes vectors is an ill-posed one in polarization formalism and represents a real disability to leverage the pure physical part of the polarization (Stokes vectors, AOLP, DOLP). This is a line of research we will investigate in future works by, for instance, projecting the Stokes vectors into the Minkowski space or the Krein space. However, before dealing with this pointed issue, a correct estimation of the Stokes parameters is paramount and this is what we have accomplished in this paper.

Acknowledgements This project was co-financed by the European Union with the European regional development fund (ERDF, 18P03390/18E01750/18P02733), by the Haute-Normandie Régional Council via the M2SINUM project and by the French Research National Agency ANR via ICUB project ANR 17-CE 22-0011-01. The authors would like to thank Dr Sylvain Faisan (ICube - MIV, Université de Strasbourg) for providing us with the code to generate artificial data in the full Stokes recovery case.

Appendix A: Pointwise Infimum of Concave Functions

Let us denote by $f(p) = \inf_{S \in \mathcal{K}} \mathcal{L}(S, p) = \inf_{S \in \mathcal{K}} \mathcal{L}_S(p)$. In our case, for each p the infimum is reached so that we could

write equivalently $f(p) = \min_{S \in \mathcal{K}} \mathcal{L}_S(p)$. Let us prove that f is concave.

We recall a preliminary result.

Theorem 3 *Let X be a set and let $f : X \rightarrow \bar{\mathbb{R}}$. The hypograph of f is defined by*

$$\text{hypo } f = \{(x, t) \in X \times \mathbb{R} \mid f(x) \geq t\}.$$

A function $f : X \rightarrow \bar{\mathbb{R}}$ is concave if and only if its hypograph is convex.

Coming back to our problem,

$$\text{hypo } f = \{(p, t) \in \mathcal{B} \times \mathbb{R} \mid f(p) \geq t\}, \tag{A1}$$

$$= \left\{ (p, t) \in \mathcal{B} \times \mathbb{R} \mid \inf_{S \in \mathcal{K}} \mathcal{L}_S(p) \geq t \right\}, \tag{A2}$$

$$= \bigcap_{S \in \mathcal{K}} \{(p, t) \in \mathcal{B} \times \mathbb{R} \mid \mathcal{L}_S(p) \geq t\}, \tag{A3}$$

which is convex as the intersection of convex sets.

Appendix B: Pointwise Infimum of Continuous Functions

Theorem 4 *Let (X, τ) be a topological space and let $f : X \rightarrow \bar{\mathbb{R}}$ be a function. Function f is upper semi-continuous if $\forall \alpha \in \mathbb{R}$, the set $\{x \in X \mid f(x) < \alpha\}$ is open.*

Let us prove that $f : p \in \mathcal{B} \mapsto \inf_{S \in \mathcal{K}} \mathcal{L}(S, p)$ is upper semi-continuous. Let $\alpha \in \mathbb{R}$. Let $p \in f^{-1}((-\infty, \alpha))$. Then, $\inf_{S \in \mathcal{K}} \mathcal{L}(S, p) < \alpha$ and there exists $\bar{S}_p \in \mathcal{K}$ such that $\mathcal{L}(\bar{S}_p, p) = \mathcal{L}_{\bar{S}_p}(p) < \alpha$. This implies that

$$f^{-1}((-\infty, \alpha)) = \bigcup_{S \in \mathcal{K}} \mathcal{L}_S^{-1}((-\infty, \alpha))$$

which is open as the union of open sets.

Appendix C: Alternative Proof to Get the Proximal Operator of τg

Consider the three-dimensional optimization problem

$$\begin{aligned} u^* &= \text{prox}_{\tau g}(u = (u_0, u_1, u_2)) \\ &= \arg \min_{\tilde{u}=(\tilde{u}_0, \tilde{u}_1, \tilde{u}_2) \in \mathbb{R}^3} \frac{1}{2\tau} \|\tilde{u}-u\|_{\mathbb{R}^3}^2 + \frac{\mu}{2} \|A\tilde{u}-I\|_{\mathbb{R}^4}^2 + i\tilde{c}(\tilde{u}). \end{aligned}$$

Using the identity

$$\begin{aligned} &v(a - b)^2 + \mu(a - c)^2 \\ &= (v + \mu)a^2 - 2a(vb + \mu c) + vb^2 + \mu c^2 \\ &= (v + \mu)\left(a - \frac{vb + \mu c}{v + \mu}\right)^2 \\ &\quad - \frac{(vb + \mu c)^2}{v + \mu} + vb^2 + \mu c^2, \end{aligned}$$

and the fact that $A^T A = \begin{pmatrix} 1 & 0 & 0 \\ 0 & \frac{1}{2} & 0 \\ 0 & 0 & \frac{1}{2} \end{pmatrix}$, the minimization problem can be equivalently restated as:

$$\begin{aligned} u^* &= \arg \min_{\tilde{u} \in \mathbb{R}^3} \alpha(\tilde{u}_0 - z_0)^2 + \beta(\tilde{u}_1 - z_1)^2 \\ &\quad + \beta(\tilde{u}_2 - z_2)^2 + i_{\bar{C}}(\tilde{u}) \\ &= \arg \min_{\tilde{u} \in \mathbb{R}^3} (\sqrt{\alpha}\tilde{u}_0 - \sqrt{\alpha}z_0)^2 + (\sqrt{\beta}\tilde{u}_1 - \sqrt{\beta}z_1)^2 \\ &\quad + (\sqrt{\beta}\tilde{u}_2 - \sqrt{\beta}z_2)^2 + i_{\bar{C}}(\tilde{u}), \end{aligned} \tag{C1}$$

with $\begin{cases} \alpha = \frac{1}{2\tau} + \frac{\mu}{2} \\ \beta = \frac{1}{2\tau} + \frac{\mu}{4} \end{cases}$, and $z_0 = \frac{\frac{1}{2\tau}u_0 + \frac{\mu}{2}b_0}{\alpha}$, $z_1 = \frac{\frac{1}{2\tau}u_1 + \frac{\mu}{2}b_1}{\beta}$
and $z_2 = \frac{\frac{1}{2\tau}u_2 + \frac{\mu}{2}b_2}{\beta}$.

We then set $\begin{cases} \tilde{u}_0 = \sqrt{\alpha}\tilde{u}_0 \\ \tilde{u}_1 = \sqrt{\beta}\tilde{u}_1 \\ \tilde{u}_2 = \sqrt{\beta}\tilde{u}_2 \end{cases}$, $\begin{cases} \bar{z}_0 = \sqrt{\alpha}z_0 \\ \bar{z}_1 = \sqrt{\beta}z_1 \\ \bar{z}_2 = \sqrt{\beta}z_2 \end{cases}$ and \bar{C} the closed convex set defined by

$$\bar{C} = \left\{ t = (t_0, t_1, t_2) \in \mathbb{R}^3 \mid t_0 \geq \sqrt{\frac{\alpha}{\beta}}\sqrt{t_1^2 + t_2^2} \right\},$$

and consider the auxiliary problem related to (C1)

$$\arg \min_{\tilde{u}=(\tilde{u}_0, \tilde{u}_1, \tilde{u}_2) \in \mathbb{R}^3} \|\tilde{u} - \bar{z}\|_{\mathbb{R}^3}^2 + i_{\bar{C}}(\tilde{u}), \tag{C2}$$

which thus amounts to computing the projection of $\bar{z} = (\bar{z}_0, \bar{z}_1, \bar{z}_2)$ onto \bar{C} . Once the (unique) solution of (C2) is obtained, it suffices to use the previous change of variable to recover the u_i^* 's.

Let us now recall the following result dedicated to orthogonal projection onto epigraphs.

Theorem 5 *Orthogonal projection onto epigraphs, taken from [34, Chapter 6, Theorem 6.36] with \mathbb{E} a Euclidean space, let*

$$C = \text{epi}(g) = \{(x, t) \in \mathbb{E} \times \mathbb{R} : g(x) \leq t\},$$

where $g : \mathbb{E} \rightarrow \mathbb{R}$ is convex. Then,

$$P_C((x, s)) = \begin{cases} (x, s) & \text{if } g(x) \leq s \\ (\text{prox}_{\lambda^* g}(x), s + \lambda^*) & \text{if } g(x) > s \end{cases},$$

where λ^* is any positive root of the function

$$\Psi(\lambda) = g(\text{prox}_{\lambda g}(x)) - \lambda - s.$$

In addition, Ψ is nonincreasing.

We invoke the previous theorem with $g(\cdot) = \sqrt{\frac{\alpha}{\beta}}\|\cdot\|_{\mathbb{R}^2}$ to obtain the formula and follow the arguments of Beck ([34, Chapter 6]) (we respect the same order in the arguments of $P_{\bar{C}}(\cdot)$ as in [34])

$$\begin{aligned} P_{\bar{C}}(\hat{z} = (\bar{z}_1, \bar{z}_2), \bar{z}_0) &= \begin{cases} (\bar{z}_1, \bar{z}_2, \bar{z}_0) & \text{if } \bar{z}_0 \geq \sqrt{\frac{\alpha}{\beta}}\|\hat{z}\|_{\mathbb{R}^2} \\ (\text{prox}_{\lambda^* \sqrt{\frac{\alpha}{\beta}}\|\cdot\|_{\mathbb{R}^2}}(\hat{z}), \bar{z}_0 + \lambda^*) & \text{if } \bar{z}_0 < \sqrt{\frac{\alpha}{\beta}}\|\hat{z}\|_{\mathbb{R}^2} \end{cases}, \end{aligned}$$

where λ^* is any positive root of the function $\Psi(\lambda) = \sqrt{\frac{\alpha}{\beta}}\|\text{prox}_{\lambda \sqrt{\frac{\alpha}{\beta}}\|\cdot\|_{\mathbb{R}^2}}(\hat{z})\|_{\mathbb{R}^2} - \lambda - \bar{z}_0$.

Let (\hat{z}, \bar{z}_0) be such that $\bar{z}_0 < \sqrt{\frac{\alpha}{\beta}}\|\hat{z}\|_{\mathbb{R}^2}$.

Recall that

$$\text{prox}_{\lambda \sqrt{\frac{\alpha}{\beta}}\|\cdot\|_{\mathbb{R}^2}}(\hat{z}) = \left[1 - \frac{\lambda \sqrt{\frac{\alpha}{\beta}}}{\max(\|\hat{z}\|_{\mathbb{R}^2}, \lambda \sqrt{\frac{\alpha}{\beta}})} \right] \hat{z}.$$

Plugging the above into the expression of Ψ leads to

$$\begin{aligned} \Psi(\lambda) &= \sqrt{\frac{\alpha}{\beta}} \left[1 - \frac{\lambda \sqrt{\frac{\alpha}{\beta}}}{\max(\|\hat{z}\|_{\mathbb{R}^2}, \lambda \sqrt{\frac{\alpha}{\beta}})} \right] \|\hat{z}\|_{\mathbb{R}^2} - \lambda - \bar{z}_0 \\ &= \begin{cases} \sqrt{\frac{\alpha}{\beta}}\|\hat{z}\|_{\mathbb{R}^2} - \lambda \frac{\alpha}{\beta} - \lambda - \bar{z}_0 & \text{if } \|\hat{z}\|_{\mathbb{R}^2} \geq \lambda \sqrt{\frac{\alpha}{\beta}} \\ -\lambda - \bar{z}_0 & \text{if } \|\hat{z}\|_{\mathbb{R}^2} < \lambda \sqrt{\frac{\alpha}{\beta}} \end{cases}. \end{aligned}$$

The unique positive root λ^* of the piecewise linear function Ψ is

$$\lambda^* = \begin{cases} \frac{\sqrt{\frac{\alpha}{\beta}}\|\hat{z}\|_{\mathbb{R}^2} - \bar{z}_0}{1 + \frac{\alpha}{\beta}} & \text{if } \|\hat{z}\|_{\mathbb{R}^2} \geq -\bar{z}_0 \sqrt{\frac{\alpha}{\beta}}, \\ -\bar{z}_0 & \text{if } \|\hat{z}\|_{\mathbb{R}^2} < -\bar{z}_0 \sqrt{\frac{\alpha}{\beta}} \end{cases},$$

resulting in

$$(\text{prox}_{\lambda^* \sqrt{\frac{\alpha}{\beta}} \|\cdot\|_{\mathbb{R}^2}}(\hat{z}), \bar{z}_0 + \lambda^*) = \begin{cases} (0, 0, 0) & \text{if } \|\hat{z}\|_{\mathbb{R}^2} < -\bar{z}_0 \sqrt{\frac{\alpha}{\beta}} \\ \left(\left(\frac{1}{1 + \frac{\alpha}{\beta}} + \frac{\sqrt{\frac{\alpha}{\beta}}}{1 + \frac{\alpha}{\beta}} \frac{\bar{z}_0}{\|\hat{z}\|_{\mathbb{R}^2}} \right) \hat{z}, \frac{\frac{\alpha}{\beta} \bar{z}_0 + \sqrt{\frac{\alpha}{\beta}} \|\hat{z}\|_{\mathbb{R}^2}}{1 + \frac{\alpha}{\beta}} \right) & \text{if } \|\hat{z}\|_{\mathbb{R}^2} \geq -\bar{z}_0 \sqrt{\frac{\alpha}{\beta}} \end{cases}$$

If we summarize the whole results, coming back to the initial variables, we see that we recover the results obtained with the necessary and sufficient KKT condition. Indeed,

- If $\bar{z}_0 \geq \sqrt{\frac{\alpha}{\beta}} \|\hat{z}\|_{\mathbb{R}^2}$ or equivalently, $z_0 \geq \sqrt{z_1^2 + z_2^2}$,

$$\begin{aligned} (\sqrt{\alpha} u_0^*, \sqrt{\beta} u_1^*, \sqrt{\beta} u_2^*) &= (\bar{z}_0, \bar{z}_1, \bar{z}_2) \\ &= (\sqrt{\alpha} z_0, \sqrt{\beta} z_1, \sqrt{\beta} z_2), \end{aligned}$$

yielding

$$(u_0^*, u_1^*, u_2^*) = (z_0, z_1, z_2).$$

- If $\bar{z}_0 < \sqrt{\frac{\alpha}{\beta}} \|\hat{z}\|_{\mathbb{R}^2}$ or equivalently, $z_0 < \sqrt{z_1^2 + z_2^2}$,

- (i) If $\bar{z}_0 \geq 0$ (or equivalently $z_0 \geq 0$), then $\|\hat{z}\|_{\mathbb{R}^2} \geq -\bar{z}_0 \sqrt{\frac{\alpha}{\beta}}$ or equivalently $\beta \sqrt{z_1^2 + z_2^2} \geq -\alpha z_0$, and intermediate computations lead to

$$\begin{aligned} u_0^* &= \frac{\alpha}{\alpha + \beta} z_0 + \frac{\beta}{\alpha + \beta} \sqrt{z_1^2 + z_2^2} \\ u_1^* &= \left(\frac{\beta}{\alpha + \beta} + \frac{\alpha}{\alpha + \beta} \frac{z_0}{\sqrt{z_1^2 + z_2^2}} \right) z_1 \\ u_2^* &= \left(\frac{\beta}{\alpha + \beta} + \frac{\alpha}{\alpha + \beta} \frac{z_0}{\sqrt{z_1^2 + z_2^2}} \right) z_2 \end{aligned}$$

- (ii) If $\bar{z}_0 < 0$ (or equivalently, $z_0 < 0$) and $\|\hat{z}\|_{\mathbb{R}^2} < -\bar{z}_0 \sqrt{\frac{\alpha}{\beta}}$ or equivalently $\beta \sqrt{z_1^2 + z_2^2} < -\alpha z_0$, then

$$(u_0^*, u_1^*, u_2^*) = (0, 0, 0).$$

- (iii) If $\bar{z}_0 < 0$ (or equivalently, $z_0 < 0$) and $\|\hat{z}\|_{\mathbb{R}^2} \geq -\bar{z}_0 \sqrt{\frac{\alpha}{\beta}}$ or equivalently $\beta \sqrt{z_1^2 + z_2^2} \geq -\alpha z_0$, then intermediate

computations lead to

$$\begin{aligned} u_0^* &= \frac{\alpha}{\alpha + \beta} z_0 + \frac{\beta}{\alpha + \beta} \sqrt{z_1^2 + z_2^2} \\ u_1^* &= \left(\frac{\beta}{\alpha + \beta} + \frac{\alpha}{\alpha + \beta} \frac{z_0}{\sqrt{z_1^2 + z_2^2}} \right) z_1 \\ u_2^* &= \left(\frac{\beta}{\alpha + \beta} + \frac{\alpha}{\alpha + \beta} \frac{z_0}{\sqrt{z_1^2 + z_2^2}} \right) z_2 \end{aligned}$$

References

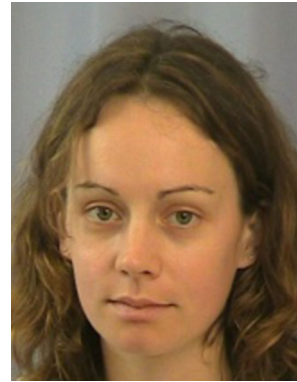
1. Wolff, L.B., Andreou, A.G.: Polarization camera sensors. *Image Vis. Comput.* **13**(6), 497–510 (1995)
2. Berger, K., Voorhies, R., Matthies, L.H.: Depth from stereo polarization in specular scenes for urban robotics. In: 2017 IEEE International Conference on Robotics and Automation (ICRA), pp. 1966–1973 (2017)
3. Zhu, D., Smith, W.A.P.: Depth From a Polarisation + RGB Stereo Pair. In: 2019 IEEE/CVF Conference on Computer Vision and Pattern Recognition (CVPR), pp. 7578–7587 (2019)
4. Morel, O., Stolz, C., Meriaudeau, F., Gorria, P.: Active lighting applied to three-dimensional reconstruction of specular metallic surfaces by polarization imaging. *Appl. Opt.* **45**(17), 4062–4068 (2006)
5. Miyazaki, D., Saito, M., Sato, Y., Ikeuchi, K.: Determining surface orientations of transparent objects based on polarization degrees in visible and infrared wavelengths. *J. Opt. Soc. Am. A* **19**(4), 687–694 (2002)
6. Rehlinger, J., Haddad, H., Deby, S., Teig, B., Nazac, A., Novikova, T., Pierangelo, A., Moreau, F.: Ex vivo Mueller polarimetric imaging of the uterine cervix: a first statistical evaluation. *J. Biomed. Opt.* **21**(7), 1–8 (2016)
7. Wang, F., Ainouz, S., Meriaudeau, F., Benshrhair, A.: Polarization-based car detection. In: 2018 25th IEEE International Conference on Image Processing (ICIP), pp. 3069–3073 (2018)
8. Aycocock, T.M., Chenault, D.B., Hanks, J.B., Harchanko, J.S.: Polarization-based mapping and perception method and system. Google Patents. US Patent 9,589,195 (2017)
9. Blin, R., Ainouz, S., Canu, S., Meriaudeau, F.: Road scenes analysis in adverse weather conditions by polarization-encoded images and adapted deep learning. In: 2019 IEEE Intelligent Transportation Systems Conference (ITSC), pp. 27–32 (2019)
10. Faisan, S., Heinrich, C., Rousseau, F., Lallement, A., Zallat, J.: Joint filtering estimation of Stokes vector images based on a nonlocal means approach. *J. Opt. Soc. Am. A* **29**(9), 2028–2037 (2012)
11. Zallat, J., Heinrich, C.: Polarimetric data reduction: a Bayesian approach. *Opt. Express* **15**(1), 83–96 (2007)
12. Zallat, J., Heinrich, C., Petremand, M.: A Bayesian approach for polarimetric data reduction: the Mueller imaging case. *Opt. Express* **16**(10), 7119–7133 (2008)
13. Valenzuela, J.R., Fessler, J.A.: Joint reconstruction of Stokes images from polarimetric measurements. *J. Opt. Soc. Am. A* **26**(4), 962–968 (2009)
14. Chambolle, A., Pock, T.: A first-order primal-dual algorithm for convex problems with applications to imaging. *J. Math. Imaging Vis.* **40**(1), 120–145 (2011)
15. Bass, M., Van Stryland, E.W., Williams, D.R., Wolfe, W.L.: *Handbook of Optics, Third Edition Volume II: Design, Fabrication and Testing, Sources and Detectors, Radiometry and Photometry*, 3rd edn. McGraw-Hill, Inc., New York (2009)

16. Terrier, P., Devlaminck, V.: Robust and accurate estimate of the orientation of partially polarized light from a camera sensor. *Appl. Opt.* **40**(29), 5233–5239 (2001)
17. Ainouz, S., Morel, O., Fofi, D., Mosaddegh, S., Benschair, A.: Adaptive processing of catadioptric images using polarization imaging: towards a pola-catadioptric model. *Opt. Eng.* **52**(3), 1–9 (2013)
18. Zubko, E., Chornaya, E.: On the ambiguous definition of the degree of linear polarization. *Res. Notes AAS* **3**(3), 45 (2019)
19. Wang, Z., Zheng, Y., Chuang, Y.-Y.: Polarimetric camera calibration using an LCD monitor. In: 2019 IEEE/CVF Conference on Computer Vision and Pattern Recognition (CVPR), pp. 3738–3747 (2019)
20. Chambolle, A.: An algorithm for total variation minimization and applications. *J. Math. Imaging Vis.* **20**(1), 89–97 (2004)
21. Pierre, F., Aujol, J.-F., Bugeau, A., Papadakis, N., Ta, V.-T.: Luminance-chrominance model for image colorization. *SIAM J. Imaging Sci.* **8**(1), 536–563 (2015)
22. Azé, D.: *Éléments d'analyse convexe et variationnelle*. Mathématiques pour le 2^{ème} cycle. Ellipses, Paris (1997)
23. Ekeland, I., Témam, R.: *Convex Analysis and Variational Problems*. Society for Industrial and Applied Mathematics, Philadelphia (1999)
24. Moreau, J.-J.: Fonctions convexes duales et points proximaux dans un espace hilbertien. *C. R. Acad. Sci.* **255**, 2897–2899 (1962)
25. Combettes, P.L., Pesquet, J.-C.: Proximal splitting methods in signal processing. In: Bauschke, H.H., Burachik, R.S., Combettes, P.L., Elser, V., Luke, D.R., Wolkowicz, H. (eds.) *Fixed-Point Algorithms for Inverse Problems in Science and Engineering*, pp. 185–212. Springer, New York (2011)
26. Kolmogorov, A., Fomine, S.: *Éléments de la Théorie des Fonctions et de l'Analyse Fonctionnelle*, 2nd edn. Mir, Moscow (1977)
27. Tang, L., Fang, Z.: Edge and contrast preserving in total variation image denoising. *EURASIP J. Adv. Signal Process.* **2016**, 1–21 (2016)
28. Wang, F., Ainouz, S., Petitjean, C., Benschair, A.: Specularity removal: a global energy minimization approach based on polarization imaging. *Comput. Vis. Image Underst.* **158**, 31–39 (2017)
29. Wang, Y., Jiang, Z., Shi, J.: Highlight area inpainting guided by illumination model. In: Fifth International Conference on Graphic and Image Processing (ICGIP 2013), vol. 9069, p. 90691 (2014). International Society for Optics and Photonics
30. Kupinski, M.K., Bradley, C.L., Diner, D.J., Xu, F., Chipman, R.A.: Angle of linear polarization images of outdoor scenes. *Opt. Eng.* **58**(8), 082419 (2019)
31. Baek, S.-H., Jeon, D.S., Tong, X., Kim, M.H.: Simultaneous acquisition of polarimetric SVBRDF and normals. *ACM Trans. Graph.* **37**(6) (2018)
32. Schechner, Y.Y., Narasimhan, S.G., Nayar, S.K.: Polarization-based vision through haze. *Appl. Opt.* **42**(3), 511–525 (2003)
33. Sarafraz, A., Negahdaripour, S., Schechner, Y.Y.: Enhancing images in scattering media utilizing stereovision and polarization. In: 2009 Workshop on Applications of Computer Vision (WACV), pp. 1–8 (2009). IEEE
34. Beck, A.: *First-Order Methods in Optimization*. Society for Industrial and Applied Mathematics, Philadelphia (2017)

Publisher's Note Springer Nature remains neutral with regard to jurisdictional claims in published maps and institutional affiliations.

Springer Nature or its licensor (e.g. a society or other partner) holds exclusive rights to this article under a publishing agreement with the author(s) or other rightsholder(s); author self-archiving of the accepted

manuscript version of this article is solely governed by the terms of such publishing agreement and applicable law.

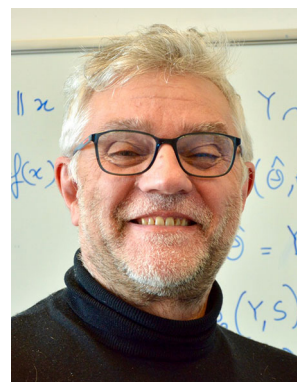


Carole Le Guyader received the French engineering degree (equivalent to M.Sc. degree) in mathematical engineering and the Post-graduate degree in engineering sciences from the National Institute of Applied Sciences (NIAS), Rouen, France, in 2002, and the Ph.D. degree in applied mathematics from NIAS, Rouen, in 2004. Her thesis was dedicated to segmentation under geometrical constraints from a theoretical and applied point of view. She held visiting research positions at the University of California, Los Angeles (Summer 2005 and 2007) and then, a position of Assistant Professor at the NIAS, Rennes. She is currently a Full Professor at the NIAS, Rouen, France. Her research interests include variational methods in image processing, hybridization of variational and machine-learning-based methods, curve and surface evolution using PDEs, viscosity solutions, and approximation of surfaces.



Samia Ainouz is a full professor at INSA Rouen Normandy. She is the head of the team Intelligent Transportation systems since June 2019. Her research area is around Multimodality for intelligent vehicle navigation including data fusion, 3D reconstruction, VSLAM. She supervised 7 PhD students around road scene analysis and autonomous navigation. Recently, she focused her research towards non-conventional imaging for autonomous navigation in adverse weather conditions

using Deep learning tools. She is currently the head of the ANR project ICUB dealing with road scene analysis in adverse weather conditions with collaboration with Peugeot PSA, Stereolabs and ImVia.



Stéphane Canu received the Ph.D. degree in applied mathematics science from the University of Technology of Compiègne (UTC), France, in 1986 where he got its first permanent position as associate professor. Founder of the Computer Science department at INSA in Rouen Normandy, he is now Professor at INSA Rouen Normandy and a member of the LITIS Research Laboratory, where he was director from 2005 to 2012. He has been also a lecturer at l'école Polytechnique from 2017 to 2020. He has been doing research for 35 years in the field of Artifi-

cial Intelligence, Machine Learning and Data Science. He is the author of more than one hundred articles with a h-index of 38 according to Google Scholar. From 2016 to 2020, he coordinated the Deep in France program funded by the ANR on the crucial question of the

energy sobriety of deep learning and now holds an IA Chair on the robustness of deep learning. He was a member of CNU 61 from 2012 to 2019, scientific officer at HCERES from 2019 to 2020 and is AI officer at MESR since 2020. He was co-chair of ECML 2022.